TAMPEREEN TEKNILLINEN YLIOPISTO
TAMPERE UNIVERSITY OF TECHNOLOGY

CLIONA SHAKESPEARE
INTERMIXING, MORPHOLOGY, AND CHARGE TRANSFER MECHANISM OF THE NI/AM-TIO2 SYSTEM

Master of Science thesis

Examiners: Prof. Mika Valden
D.Sc. Harri Ali-Löytty
Examiner and topic approved
in November 2018

ABSTRACT

CLIONA SHAKESPEARE: Intermixing, morphology, and charge transfer mechanism of the Ni/am-TiO2 system
Tampere University of Technology
Master of Science thesis, 50 pages
November 2018
Master's Degree Programme in Science and Engineering
Major: Advanced Engineering Physics
Examiner: Prof. Mika Valden, D.Sc. Harri Ali-Löytty
Keywords: solar water splitting, xps, spectromicroscopy, NanoESCA, charge transport

In this work, the intermixing of a Ni cocatalyst on amorphous TiO_2 during vacuum annealing was studied. A sample was prepared with a finger pattern of Ni deposited for 10 s via lithography on 30 nm of amorphous ALD-deposited TiO_2 atop an n-Si substrate, then reduced via cumulative annealing in ultrahigh vacuum conditions. The nickel started out oxidised, then reduced when annealed to 400°C, after which it started diffusing into the Si bulk, revealed by impedance spectroscopy. At 900°C it had disappeared from the surface. XPS of Ti revealed that the Ni reduced first, leading to greater concentrations of Ti^{4+} at the fingers than between them. Ni does not diffuse laterally, and the finger pattern remains present up to 900°C in the work function image, despite the Ni all disappearing from the surface before then. Separate samples were prepared for photoelectrochemical measurements, revealing that the 400°C annealed sample produced significantly better photocurrent for water oxidation than the original or the 800°C annealed sample. This suggests that the Ni diffuses into the TiO_2 film and increases its charge transport capacity upon heating. At 800°C, there is insufficient Ni on the surface to act as a catalyst, and an insulating SiO_2 film has formed between the TiO_2 and Si, inhibiting charge transport.

TIIVISTELMÄ

CLIONA SHAKESPEARE: Sekoittuminen, morfologia, ja varauksensiirtomekanismi nikkeli-titaanidioksidi -systeemissä
Tampereen teknillinen yliopisto
Diplomityö, 50 sivua
Marraskuu 2018
Teknis-luonnontieteellinen koulutusohjelma
Pääaine: Teknillinen fysiikka
Tarkastajat: Prof. Mika Valden, TkT Harri Ali-Löytty
Avainsanat: water splitting, röntgenviritteinen fotoelektronispektroskopia, spektromikroskopia, NanoESCA, varauksensiirto

Tässä työssä tutkittiin Ni-kokatalyytin sekoittumista amorfisen TiO_2:n kanssa tyhjiöhehkutuksessa. Näyte valmistettiin kasvattamalla sormikuvio Ni:ä litografisesti 10 s ajan amorfiselle ALD-kasvatetulle TiO_2:lle, joka oli n-Si -substraatin päällä, jonka jälkeen Ni pelkistettiin kumulatiivisella hehkutuksella ultrasuurtyhjiöolosuhteissa. Nikkeli oli aluksi hapettunut, mutta pelkistyi 400°C:een lämmitettäessä, jolloin se alkoi diffusoitua Si bulkkiin, mikä näkyi impedanssispektroskopiatuloksissa. 900°C:ssa Ni oli kadonnut pinnalta. Titaanin XPS paljasti, että Ni pelkistyi ennen Ti:a, johtaen suurempaan Ti^{4+}–konsentraatioon sormien kohdalla, kuin välissä. Erilliset näytteet valmistettiin valosähkökemiallisiin mittauksiin, jotka paljastivat, että 400°C:ssa lämmitetty näyte tuotti huomattavasti parempaa valovirtaa veden hajottamiseen, kuin alkuperäinen tai 800°C:ssa lämmitetty näyte. Täten lämmitettäessä Ni diffusoituu TiO_2-ohutkalvoon ja parantaa sen varauksensiirtokykyä. 800°C:ssa pinnalla ei ole tarpeeksi nikkeliä katalyysiin ja TiO_2:n ja piin väliin on muodostunut eristävä SiO_2-kerros, joka estää varauksensiirtoa.

PREFACE

I wish to thank my advisors, Prof Mika Valden and Dr Harri Ali-Löytty, for giving me an interesting topic on a short warning and then stepping back and giving me free rein. I knew their assistance would always be there should I need it.

While the responsibility for this project has been mine alone, science is by nature a collaborative endeavor. Dr Ali-Löytty deserves my thanks also for designing the lithography mask used in making the Ni/am-TiO_2/n-Si samples measured in this work. The TiO_2 films measured in this study were deposited by MSc Jesse Saari, and the UV lithography of the Ni pattern done by MSc Timo Aho. The excellent SEM picture was taken by BSc Riina Ulkuniemi, and MSc Lauri Palmolahti assisted in setting up the PEC measurements. I also wish to thank MSc Markku Hannula for teaching me how to use NanoESCA and graciously allowing me to use his Matlab scripts so I could avoid reinventing the wheel, as well as granting me access to his vast library of prior reference measurements.

Thanks also go to Dr Kimmo Lahtonen for being an excellent teacher and MSc Saari for holding my hand at the beginning of my journey into experimental science. In addition to the aforementioned, I wish to acknowledge Dr Leena Vuori, MSc Bela Bhuskute, and Tuomas Tinus for contributing to a positive environment in the lab.

Lastly, I would like to acknowledge my parents, Dr John and Dr Tarja Shakespeare, for planting and then nurturing in me the seed of curiosity, and knowing when it is time to let go. Without them, I would not be where I am now.

Tampere, 5.11.2018

Cliona Shakespeare

CONTENTS

LIST OF FIGURES

LIST OF TABLES

LIST OF ABBREVIATIONS AND SYMBOLS

AC	Alternating current
ALD	Atomic layer deposition
BE	Binding energy
CA	Constant potential amperometry
CAE	Constant analyzer energy
CB	Conduction band
CCD	Charge-coupled device
CHA	Concentric hemispherical analyzer
eV	Electron volt; 1 eV = 1.602 176 621 $\times 10^{-19}$ J
FRA	Frequency response analysis
HER	Hydrogen evolution reaction
IMFP	Inelastic mean free path
KE	Kinetic Energy
Kα	Spectral line of characteristic radiation
MCP	Microchannel plate
NHE	Neutral hydrogen electrode
OER	Oxygen evolution reaction
PEEM	Photoemission electron microscopy
PES	Photoelectron spectroscopy
RSF	Relative sensitivity factor
TDMAT	Tetrakis(dimethylamino)titanium
TUT	Tampere University of Technology
UHV	Ultrahigh vacuum
UPS	Ultraviolet photoelectron spectroscopy
UV	Ultraviolet light
VB	Valence band
XPS	X-ray photoelectron spectroscopy

c_a	Concentration of species a
C_b	Capacitance of inner coating layer
C_p	Capacitance of outer coating layer
d	Spacing of atomic planes
d_{obj}	Distance between sample and objective
e	Elementary charge; $e = -1.602\ 176\ 621 \times 10^{-19}$ C
$\mathbf{E}_{acc}$	Accelerating electric field
E_B	Binding energy

E_F	Fermi energy
E_K	Kinetic energy
E_v	Vacuum energy level
h	Planck's constant
I	Intensity
I_0	Unattenuated intensity
J	Radiation flux impacting analysis region
K_f	Instrument factors
n	Diffraction order
R_b	Resistance of inner coating layer
R_p	Resistance of outer coating layer
R_s	Resistance of solution
V_{ext}	Electric potential of extractor
V_{spl}	Electric potential of sample
z	Depth from which electrons emanate
α_{pc}	Photoionization cross-section
ϵ_0	Vacuum permittivity; ϵ_0 =8.854 187 817 $\times 10^{-12}$ Fm^{-1}
θ	Angle
λ	Wavelength
λ_{IMFP}	Inelastic mean free path of electrons in a substance
ν	Frequency
Φ	Work function
ϕ	Diffraction angle

1. INTRODUCTION

In a world facing the ever-increasing warning signs of global warming, the need for non–carbon–emissive sources of energy is huge. The needs and thus solutions for each application are different, but one promising way of storing the energy of the Sun is by using it to split water into oxygen and hydrogen, which can be stored and burned back into water for energy. When the reaction of water into oxygen and hydrogen happens catalyzed by sunlight on a surface, it is called solar water splitting.

One means of achieving this dream of solar water splitting is the humble TiO_2. It was the first material with which solar water splitting was developed, and remains a common benchmark [6]. Its band gap is unfortunately wide for efficient water splitting, and it can only convert ultraviolet light to hydrogen. Many groups have attempted to investigate how to narrow the band gap, either with doping or structuring, as TiO_2 is cheap and prolific in the Earth's crust, unlike competitior materials with better solar to hydrogen conversion efficiency. Another application for it is using it as a means of protecting other photocatalysts from dissolving under water splitting conditions [7].

Beyond simple band gap size, the details of the energy bands and electron transfer affect the solar to hydrogen conversion efficiency. If photogenerated electron–hole pairs immediately recombine, they cannot be used to produce hydrogen. Altering the band structure of the system with a metal cocatalyst helps delocalize the excited electrons from the formed holes, as well as improves the charge transfer properties of the TiO_2. While several noble metals are successfully used, a true breakthrough would involve an earth-abundant cocatalyst, such as nickel, so that the end product would be economically viable.

Nickel has been deposited onto catalyst surfaces in many configurations, for example as nickel catalyst islands which have been oxidised partially, so that the core of the island is still metallic to enable charge transfer [8]. In later years, this has been further pursued with thin layers of Ni [9]. Investigation of a plausible, easy means of nickel deposition, and how it compares to this prior research, as well as how the

nickel behaves on the TiO_2, both on photocatalyst and catalyst protector surfaces, is thus a productive avenue of research.

As water splitting is a form of catalysis and thus happens on surfaces, the means of research should be surface-sensitive as well. Photoelectron spectroscopy has a suitable information depth for investigation of the surface layers, and can distinguish both between elements and between chemical states of the same element, yielding information on the chemical composition. Spectromicroscopic techniques will tell that as a function of spatial coordinate, revealing potential lateral intermixing of nickel into the TiO_2 matrix. Information on how the nickel affects charge transfer is best acquired via impedance spectroscopy.

In this work, the vacuum reduction of Ni fingers on amorphous TiO_2 atomic layer deposited atop n-Si(100)(P) was studied to investigate its reduction behavior and charge transfer mechanisms. This was done with x–ray photoelectron spectromicroscopy and impedance spectroscopy. X–ray photoelectron spectroscopy is ideal for studying the surface active in water splitting due to its surface sensitivity, and with spectromicroscopic techniques lateral diffusion of elements can be investigated. Impedance spectroscopy is a frequently–used means of gleaning information on charge transfer mechanisms. The results of this study can be used to further understand Ni-patterned amorphous TiO_2 atop n-Si as a solar water splitting catalyst, and provide a roadmap for future optimization.

2. SOLAR WATER SPLITTING

Water splitting is the splitting of water into its component parts of hydrogen and oxygen, catalyzed by sunlight. The hydrogen is gathered for later use as an environmentally friendly fuel. [10]

TiO_2 was the first material with which water splitting was demonstrated and a common reference to which new materials are compared [6]. As such, in addition to studies searching for other photocatalysts for water splitting, there have been several studies on how to improve the photocatalytic properties of titania, whether by modification [11], doping [12], or addition of cocatalysts [9]. Amorphous TiO_2 can also be used to coat Si, GaAs, and GaP photoanodes to prevent photocorrosion in the aqueous environment [7]. Such systems can also be further improved by addition of cocatalysts, such as Ni [7]. An intriguing means is "self–doping", where Ti^{3+} defect states and interstitial Ti atoms contribute to a density of states tail that reduces the band gap and thus increases the maximal water splitting efficiency [13]. These Ti^{3+} defect states also increase the charge transport properties of amorphous TiO_2 [14].

2.1 Principles

At its most basic, water splitting is done by an incoming photon exciting an electron from the valence band (VB) to the conduction band (CB) of a semiconductor. This is described in Figure 2.1. The conduction band electron is transferred to be used in the hydrogen evolution reaction (HER) and the valence band hole is filled by an excess electron liberated in the oxygen evolution reaction (OER), resetting the system. The HER happens at 0 V vs normal hydrogen electrode (NHE) and the OER at 1.23 V vs. NHE, so the conduction band of the material needs to be at potential greater than or equal to 0 V and the valence band at potentials lesser than or equal to -1.23 V [10]

The reactions that form H_2 and O_2 depend on the pH of the electrolyte. In an acidic

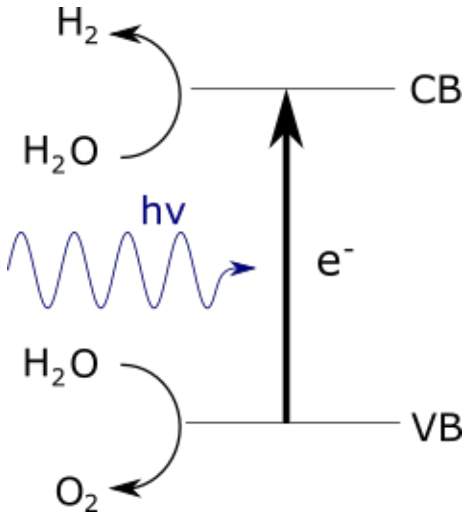

Figure 2.1 *A schematic of single-material photocatalyzed water splitting. A photon excites an electron from the VB to the CB. The hole left behind is filled with an electron liberated in the OER, while the excited electron is used in the HER to reduce water into H_2. The reactions that form H_2 and O_2 depend on the pH.*

medium, H_2 and O_2 are produced from H^+ and H_2O [15]:

$$2H^+ + 2e^- \longrightarrow H_2 \tag{2.1}$$

$$H_2O \longrightarrow 2H^+ + \frac{1}{2}O_2 + 2e^- \tag{2.2}$$

and in an alkaline or neutral medium, H_2 and O_2 are produced from H_2O and OH^- [15]:

$$2H_2O + 2e^- \longrightarrow H_2 + 2OH^- \tag{2.3}$$

$$2OH^- \longrightarrow H_2O + \frac{1}{2}O_2 + 2e^- \tag{2.4}$$

While the reaction mechanism for H_2 formation in alkaline media is not yet known, in acidic media it happens in two steps, with the intermediate phase being adsorbed H_{ads} that has received one electron. Two H_{ads} may react to form H_2, or H_{ads} may react with a H^+ in the solution and receive another electron to form H_2. [15]

2.2 Materials for water splitting

The VB and CB of the photocatalyst must straddle the OER and HER potentials, so the band gap of the material must be at least 1.23 eV [10]. A further limitation is that materials with suitable band gaps might not have their VB and CB at the correct

potentials, meaning that biasing of the water splitting catalyst is required [10]. Additionally, overpotentials are required to surmount the activation barriers of the HER and OER, i.e. the CB potential must be at a potential greater to 0 V vs. NHE and the VB potential must be at a potential lesser than −1.23 V vs. NHE so that electrons can always flow downhill [10]. The slowest reaction is the OER, which is a four-electron process, so overpotentials are most needed there [16]. The valence band hole and conduction band electron must also be spatially delocalized to prevent instant recombination [16].

In addition to the challenges of finding a material that is capable of photocatalysis, the material must be stable under photocatalytic conditions [10]. A number of otherwise suitable materials corrode in aqueous environments either with or without illumination [17]. Coatings must be deployed, or the electronic configuration of the surface altered, to protect against corrosion [16].

In the absence of a material with VB and CB values perfect for water splitting, we can only use combinations of materials. Common constructions are an otherwise single–band–gap device with cocatalysts for catalyzing the HER and/or the OER, and the "Z scheme", where one material (with optional cocatalyst) catalyzes the OER and is connected via an electron mediator to another material (with optional cocatalyst) that catalyzes the HER. The band structure of the Z scheme water splitting device is illustrated in Figure 2.2. This consumes two electrons for total water splitting instead of one, but is often the only realistic option. [18]

The construction of Z scheme water splitting devices is time–consuming, and often it is best to be able to optimize the photocathode and photoanode separately. The photoelectrochemical (PEC) responses of the half–cell materials must also overlap on the current vs voltage plot, since it is at that intersection that the resultant water splitting device will operate. If there is no voltage where photoanode and photocathode produce the same current under photoelectrochemical measurements, the sum device will not produce current. The photoelectrochemical properties of the half–cell materials can be investigated in a three–electrode PEC cell. [10]

Si is a photocatalyst with a small band gap, and thus capable of using most of the solar spectrum to split water [6]. It is used as a photocathode to catalyze the HER in Z scheme water splitting devices [19]. Its band gap is indirect [20], so the excited electron is immediately delocalized from the hole it leaves behind. Unfortunately, Si is unstable in water under illumination, and requires passivation or surface alteration [17]. One means of passivating Si is to coat it with amorphous TiO_2 films, which are suitable for protecting Si photocatalysts while enabling charge transport through

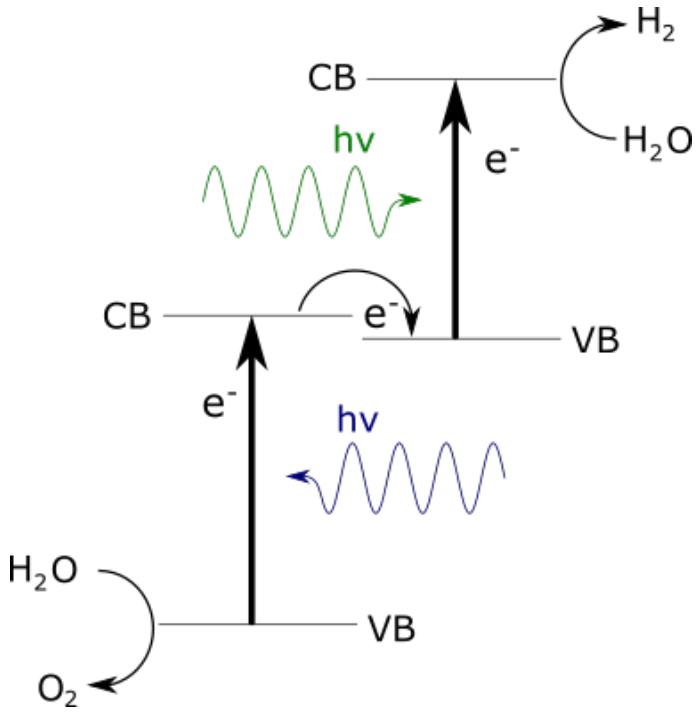

Figure 2.2 *A schematic of the principle behind the "Z scheme" water splitting device. One photon excites an electron from the VB to the CB of the OER catalyst; the hole this leaves behind is filled in the OER. The electron finds a hole at a lower energy level in the VB of the HER catalyst, and moves over through the electron mediator. Another photon excites it from the VB to the CB of the HER catalyst, where it is used to reduce water in the HER.*

them, in addition to TiO_2 being a photocatalyst in its own right [7, 21]. Passivation with electronically "leaky" tunnel oxides also yields better photocurrents than passivation with noble metals, noble metal silicides [21].

2.3 Nickel based cocatalyst in water splitting

To aid with photocatalysis, a cocatalyst can be used to alter the electronic structure of the surface to assist spatial delocalization of the hole and electron, or add auspicious surface sites that may lower the activation energy of either reaction. As the process is a surface process, most cocatalysts are in nanoparticle form to maximize the surface area and minimize volume. Additionally, a cocatalyst is one means of protecting the semiconductor from photocorrosion. [16]

Ni is a cocatalyst for the HER and NiO a cocatalyst for total water splitting, i.e. both the HER and OER [16]. Metallic Ni forms a Schottky barrier on the semiconductor surface, aiding with charge separation [16]. While metallic Ni requires a significant overpotential to drive the hydrogen evolution reaction, its oxides are more readily

usable [16]. Ni–loaded TiO_2 produces 135 times as much H_2 as pure TiO_2 [22], and Ni–decorated TiO_2 is only three times less efficient than Pt-decorated TiO_2 [23]. Other non-noble–metal cocatalysts include Fe, Co, Cu, Mo, and W [15].

In the 80s, Domen *et al.* developed a means of Ni cocatalysis by depositing nanoclusters of NiO_x on a TiO_2 surface, then reducing the oxide into metallic Ni by annealing in a reducing atmosphere, and oxidizing the surface of the metallic Ni by annealing in an oxidizing atmosphere. This creates NiO shells with metallic Ni centers. The NiO layer impedes both the back reaction of O_2 and H_2 back into water and the further oxidation of Ni. The metallic Ni center enhances charge carrier transport between the active NiO and the photocatalyst semiconductor. [8]

Ni has also been used as a cocatalyst on Si. Zhao *et al.* first protected n-Si from photocorrosion with a porous SiO_2 layer, with Ni present both on the surface as a patterned catalyst and as tendrils in the SiO_2 layer to improve the charge transport properties of the SiO_2 layer [24]. Compared to Pt cocatalysts on Si, Ni is not as good a cocatalyst, but due to its Earth–abundant nature is an appealing cocatalyst, either by itself or alloyed with other Earth–abundant elements [25].

3. ATOMIC LAYER DEPOSITION

3.1 Principles

Atomic layer deposition (ALD) is type of chemical vapor deposition that produces conformal, pinhole–free thin films, the thickness of which can be precisely controlled on the Ångström or monolayer scale. The typical ALD reaction has two components, which are pulsed onto the surface one after the other. The reactions the chemicals (precursors) have with the surface must be self-limiting to achieve exactly one monolayer of coverage. As ALD precursors are gas-phase chemicals, they can fill every available surface site even on large substrates without the need for line-of-sight, and produce a conformal film. [26]

The basic process of ALD is visualized in Figure 3.1. Precursor A is pulsed into

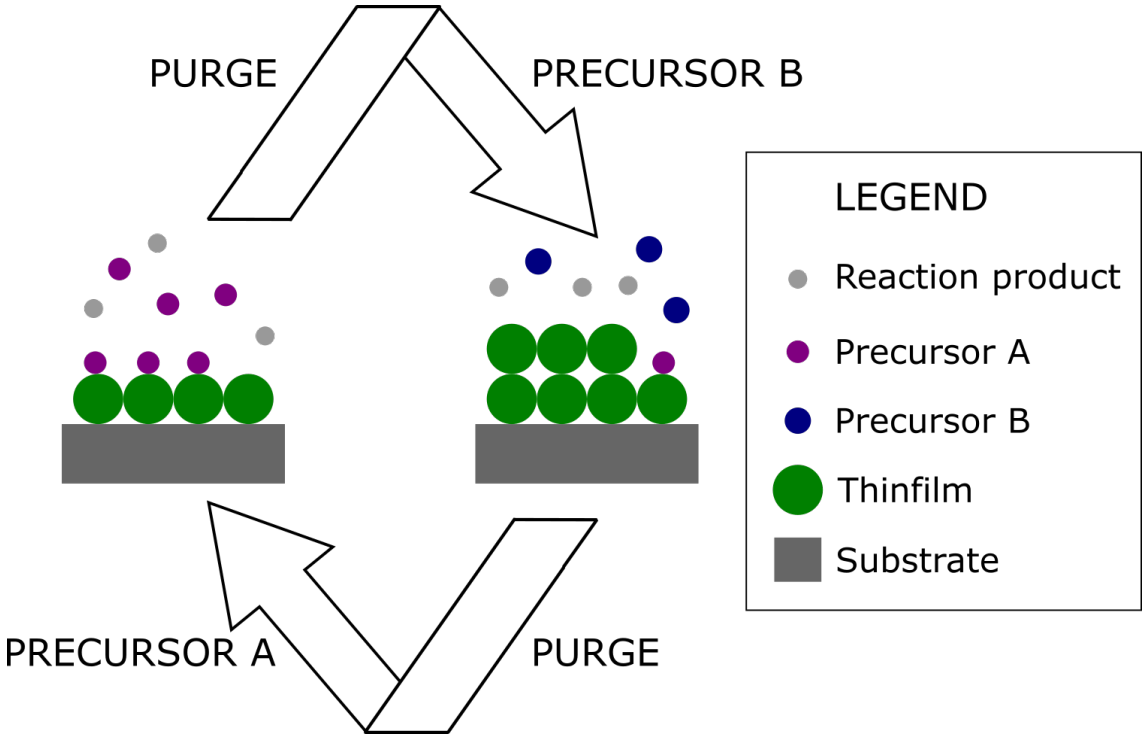

Figure 3.1 *A schematic diagram of the ALD process. After each pulse of precursor, excess reagents are purged from the system. After Kääriäinen et al. [1].*

the reaction chamber, wherein it reacts with the surface. After the surface has been covered, the excess reagent and potential reaction products are pumped out of the reaction chamber. Precursor B is then pulsed in, where it reacts with the surface species formed by precursor A to form the desired thin film chemical. After this, the excess reagent and potential reaction products are pumped out of the reaction chamber, and the cycle is repeated. [1]

ALD was first invented in Finland in the 1970s by Tuomo Suntola, who developed a means of growing ZnS. At first, ALD was referred to as atomic layer epitaxy, but as most films grown are not epitaxial with the underlying surface, the term ALD caught on in 2000. [26]

3.2 Execution

As ALD precursors are in the gas phase when they impact the substrate, the best way to ensure an oversupply of precursor molecules and a homogenous surface is to have an inert carrier gas flow past the precursor source and pick up the necessary molecules before depositing them to the reaction chamber. Using a carrier gas also enables the efficient purging of excess reactants, ensuring that the reaction will only happen on the surface, rather than the precursor molecules reacting in the space above and around it. [26]

Consideration must be taken when choosing the precursor materials as well. They must have high vapor pressures and an "ALD window": a temperature range where ALD growth is stable, below which the reactions are incomplete and above which the precursors desorb rather than react. [26]

3.3 ALD of titania from TDMAT

The growth of TiO_2 from tetrakis(dimethylamino)titanium (TDMAT) ($Ti[N(CH_3)_2]_4$) and water (H_2O) precursors has been studied by Head *et al.* with photoelectron spectroscopy [27]. Where * denotes a surface species and — an adsorbed species, the half cycle reactions are:

$$Ti(OH)_2^* + Ti[N(CH_3)_2]_4 \longrightarrow TiO_2 + — Ti[N(CH_3)_2]_2^* + 2HN(CH_3)_2 \quad (3.1)$$

$$TiO_2 + — Ti[N(CH_3)_2]_2^* + 2H_2O \longrightarrow Ti(OH)_2^* + 2HN(CH_3)_2 \quad (3.2)$$

Each cycle of pulses should thus produce a monolayer of titania. Reality, however, is rarely so simple. ALD precursors do not perfectly cover the surface, leading to growth rates of less than a monolayer per full cycle, and the presence of Ti suboxides. [27]

ALD of amorphous TiO_2 extends to deposition temperatures of around 250°C, above which H_2O desorbs, and the growth mode changes to chemical vapor deposition [28]. Growth of amorphous TiO_2 layers starts even at 50°C [29]. The ALD window proper, where the growth rate in atomic layers per cycle is linearly dependent on the temperature, lies between these temperatures, at 100–200°C [30]. The properties of ALD TiO_2 depend heavily on the deposition temperature [28].

4. PHOTOELECTRON SPECTROSCOPY

The basis of photoelectron spectroscopy (PES) is the photoelectric effect, which was first discovered by Heinrich Herz in the 1880s, and explained by Albert Einstein in 1905 as arising from a photon transferring its energy to an electron. Due to electron collection requiring an ultrahigh vacuum (UHV), it took until 1967 for Kai Siegbahn to pioneer an instrument based on the photoelectric effect capable of speciation analysis, an achievement acknowledged by the Nobel Committee with the 1981 Nobel Prize in Physics. PES is typically categorized by the wavelength of the exciting light. [3]

In X-ray photoelecton spectroscopy (XPS), a sample is subjected to a flux of low-energy monoenergetic x-rays, which detach electrons from the sample [3]. The kinetic energy of the electrons is the difference in energy between the final state and initial state of the system less the work function, which is the amount of energy the electron must be given to escape from the electron sea at the Fermi energy E_F into the vacuum E_v [31]. The initial state of the system depends on not only the orbital (eg. 1s) the electrons originate from, but also the element in question and the chemical state of the element, making XPS a useful tool for chemical analysis of surfaces [32].

Ultraviolet photoelectron spectroscopy (UPS) has the sample irradiated with monoenergetic ultraviolet photons [3]. Like XPS, the kinetic energy of the electrons depends on the difference between initial and energy of the final states [33]. A key difference to XPS is that UPS does not access the core levels due to insufficiently energetic inciting radiation, and is more sensitive to valence level electrons, making it a good tool to probe the valence band and the work function of the material [31].

4.1 Principles

The photoelectric effect describes what happens in a material under illumination: when hit by photons, which have energy $E = h\nu$, an electron will detach if and only if the energy of the photon $h\nu$ is greater than the energy that binds the electron to the nucleus. To detach the valence electrons of most elements requires for one to

venture into the ultraviolet; for core level electrons, x-ray radiation is necessary. [3]

PES requires an apparatus with a source of monoenergetic photons — usually Mg or Al Kα for XPS and He gas discharge fluorescence for UPS — a UHV chamber that holds the sample without contaminating the surface, an electrostatic lens system to gather and focus the emitted electrons, and an energy analyzer to resolve the spectrum [3]. In modern times, the most used energy analyzer is the concentric hemispherical analyzer, which sends the electrons through a curved electric field to select only the electrons of the energy of interest [3]. To acquire a full spectrum, either the accelerating potential of the lens system or the potential of the hemispherical analyzer must be changeable [3]. A more full description of the XPS apparatus can be found in Section 4.6.

4.2 Photoelectrons

The binding energy of the photoelectron is calculated using the Einstein relation, described in Equation 4.1, where E_B is the binding energy, $h\nu$ is the energy of the inciting photons, E_K is the measured kinetic energy of the electrons, and Φ is the work function in eV. [31]

$$E_B = h\nu - E_K - \Phi \tag{4.1}$$

The binding energy of the photoelectron depends primarily on the element and orbital it originates from, and can be approximated to be the negative of the energy of the initial state of the electron, so that for an electron from state k, $E_B(k) = -\epsilon_k$. This approximation is known as Koopmans' theorem. [31]

However, the kinetic energy of the photoelectron depends also on the final state, so changes in initial or final state can affect the measured binding energy [31]. The one-electron picture of Koopmans' theorem also neglects relativistic effects and electron correlation, in addition to relaxation effects stemming from changes to the final state [31]. A more accurate expression for the measured binding energy of an electron is equation 4.2, where ϵ_k is the energy of the state, $\delta\epsilon_{relax}$ is the energy change associated with relaxation effects, $\delta\epsilon_{relat}$ is the energy change associated with relativistic effects, and $\delta\epsilon_{corr}$ is the energy change associated with electron correlation effects [31].

$$E_B(k) = -\epsilon_k - \delta\epsilon_{relax} + \delta\epsilon_{relat} + \delta\epsilon_{corr} \tag{4.2}$$

Effects that alter the measured binding energy can thus be broadly categorized into initial and final state effects. Initial state effects refer to any effect arising from the

state of the atom as it was before photoelectron emission, i.e. effects affecting ϵ_k. Initial state effects include the chemical state of the atom—the change in charge density around the electron—and spin-orbit splitting. [3]

The chemical state of the atom affects the electron density around it, and when interatomic effects dominate, an increase in electron density will show as a decrease in binding energy due to Coulombic repulsion. The position of the peak can thus be used to glean information on the chemical state of the sample. This is the basis of the use of PES in speciation and chemical analysis. [3]

Final state effects come from the polarization or rearrangement induced by the core hole left by photoelectron emission [3]. The intensity of their influence on the spectrum depends on the core hole lifetime—the shorter the core hole lifetime, the stronger the effects, as the core hole decays during the photoelectron emission process [3]. Such relaxation effects can be divided into shake-up and shake-off effects [3]. Photoelectrons may also lose energy by exciting surface plasmons [3]. While relaxation effects are present in both UPS and XPS, they tend to be significantly smaller for UPS [31].

Shake-up peaks form when the core hole relaxation induces a valence band electron to excite to the conduction band, so the ion left behind by photoelectron emission is not in the ground state [32]. As this consumes energy from the photoelectron, the shake-up peaks manifest at higher binding energies (lower kinetic energies), either as discrete peaks or main peak asymmetry, depending on the energy resolution of the spectrometer [3]. The difference in energy of the shake-up peak and the main photopeak is the difference in energy of the ground state and the excited state [32]. Shake-up peaks are common for transition metals [34].

The shake-off process is similar to the shake-up process, except that the electrons depart the system of bound levels and are "shaken off" the atoms into the vacuum. Photoelectrons in systems that undergo shake-off processes become part of the electron background at higher binding energies to the main photopeak, like inelastically scattered photoelectrons do. Rarely are there discrete shake-off peaks. [3]

Plasmons are oscillations in the near-E_F electrons that form when conduction band electrons move to compensate for a change in charge density, then overshoot their mark and set up an oscillation at the preferred frequency of the electrons, which depends on the density of free electrons. Plasmon losses are seen in materials which have a high density of electrons near E_F, for example elemental Mg, Al, and Si. [3]

Auger electrons, first discovered by Lise Meitner in 1922, are a form of core hole

relaxation [31]. An electron from a higher orbital with binding energy E_B enters the core hole at a level with binding energy E_A, and donates the excess energy to a separate electron with binding energy E_C, which is then ejected if the energy is large enough [32]. The kinetic energy E_K of this Auger electron can be found in equation 4.3 [3].

$$E_K = E_A - E_B - E_C \tag{4.3}$$

This kinetic energy is independent of the process that caused the initial core hole. As Auger emission is a three-electron process, H and He are undetectable. Additionally, as atomic number Z increases, the probability of the core hole relaxing via x-ray fluorescence increases. [31]

4.3 Surface sensitivity

Due to the short attenuation length of electrons in matter, only the electrons emitted in the topmost atomic layers make it out of the sample and into the analyzer [32]. The signal comes from within 10 nm of the surface [3]. (The x-ray penetration depth of the soft x-rays used in XPS is much longer, around 1–10 μm [32], and can be ignored in discussion of surface sensitivity.) This is the basis of the surface sensitivity of the PES method, and the reason why measurements must be conducted in UHV conditions. The attenuation of electrons can be calculated using the Beer-Lambert law, shown as Equation 4.4, where I_0 is the initial, unattenuated intensity of the signal, z is the distance traversed, λ is the wavelength of the electrons, and θ is the angle [3].

$$I_z = I_0 \mathrm{e}^{-z/\lambda \sin\theta} \tag{4.4}$$

The inelastic mean free path (IMFP) describes how long a distance on average the electrons can travel experiencing only elastic collisions. Should an electron experience an inelastic collision, its kinetic energy will change by an arbitrary amount, and it will become part of the inelastic background rather than a photoelectron peak. The IMFP length depends on the energy of the electron, as shown in Figure 4.1. [3]

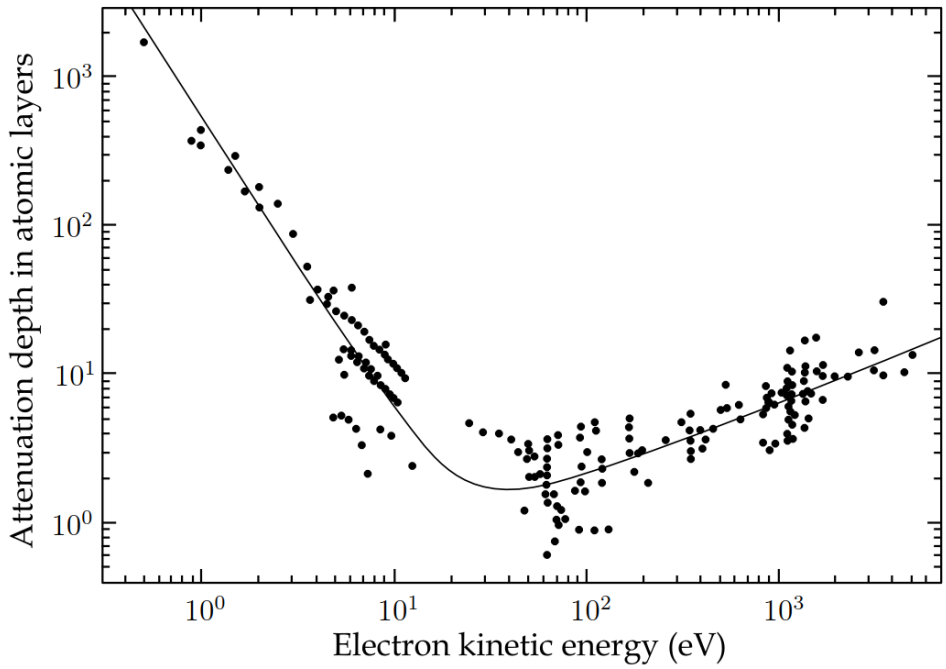

Figure 4.1 *The universal curve showing the inelastic mean free path of electrons in a solid as a function of kinetic energy. The points are measured results in different elements. After Seah and Dench [2].*

4.4 Work function

The work function Φ is a quality of the surface. It is the amount of energy it takes to detach an electron from the surface into the vacuum so that the electron and surface are infinitely far away [3]. Its value is the difference between the vacuum energy E_v and the Fermi energy E_F, according to Equation 4.5 [31].

$$\Phi = E_v - E_F \tag{4.5}$$

The vacuum energy can also be written using the surface dipole contribution $D = V(\infty) - V(-\infty)$, i.e. the difference betweeen the electrostatic potential energies of the vacuum infinitely far away and the potential infinitely deep in the bulk [31]. Choosing our scale so that the potential in the bulk, $V(-\infty)$, is 0, we get $\Phi = D - E_F$, and can see that the work function has a surface and bulk contribution [31]. The surface dipole arises from electron wave functions extending beyond the surface due to kinetic energies, so the work function is sensitive to changes in surface topography and chemistry [33].

The work function is important for determining the electronic structure of contacts [33]. When two conductors are brought next to each other, a contact potential $V_{AB} = \frac{1}{e}(\Phi_A - \Phi_B)$ will form, resulting in a charge differential at the interface [33]. For a metal and a semiconductor in contact, the Fermi levels E_F align, and the contact potential formed causes band bending in the semiconductor [20]. This forms a rectifying junction that only lets charge carriers through in one direction [20].

$$\delta\Phi = \sqrt{\frac{e}{4\pi\epsilon_0}}\sqrt{\mathbf{E}_{acc}} \tag{4.6}$$

It is possible to alter the potential of the electrons outside the surface with an electric field in e.g. immersion lens microscopy. This causes a Schottky effect that alters the surface dipole, so that the resulting change in the work function $\delta\Phi$ is according to Equation 4.6, where e is the elementary charge, ϵ_0 the vacuum permittivity, and $\mathbf{E}_{acc}$ the accelerating electric field. For the NanoESCA instrument used in this study, $\mathbf{E}_{acc} = \frac{V_{ext}-V_{spl}}{d_{obj}}$, where V_{ext} and V_{spl} are the potentials of the extractor and sample, respectively, and d_{obj} the objective lens distance. [35]

4.5 Spectromicroscopy

It is on occasion useful to know the spatial distribution of an element or the spatial differences in work function. For that, the best technique is imaging PES, also known as spectromicroscopy, which allows for the mapping of how the signal intensity depends on the position on the 2D plane. The two methods of spectromicroscopy are sequential and simultaneous pixel measurement. In the former, the image is formed by measuring the intensity of a single pixel at a time, rastering until an image is formed. In the latter, the whole field of view is measured at once with for instance a CCD. [3]

For both cases, analysis may be restricted to a single energy value, or multiple images may be taken as a scan through the energy range [3]. Measuring more than one energy allows for image processing, such as background subtraction or peak fitting, allowing for better signal detection and chemical state mapping [36].

Advances in lateral resolution and image acquisition speed have made it possible to analyze the binding energies in a more detailed fashion. This, in turn, has opened several new topics for exploration. High lateral resolution spectromicroscopy has revealed that the band bending and Schottky barriers associated with semiconductor

junctions are inhomogenous on the microscale, which has far-reaching consequences for electronics (it is the weakest barrier which dominates, not the average) and forces rethought of the theory of semiconductor interfaces. The study of the periodicity of sub-monolayer adsorbate systems and their pressure-dependence gives insight into the potential tuning of the nanopatterned surfaces for usage. The effect of different nanotexturings and the ability of different elements to block diffusion can also be studied by high-resolution spectromicroscopy of the diffused element. [37]

4.6 Elemental quantification

One of the great benefits of PES is its ability to give quantitative data of elemental and chemical concentrations. This is possible even without measuring an extensive set of reference samples. [3]

With quantification, the thing one most needs to bear in mind is that the probability of photoelectron emission is element- and orbital-dependent. When bombarded by a flux of photons, the amount of photoelectrons each orbital of each species emits will depend on the photoionization cross-section. The intensity of the measured electron signal I depends on the incoming x-ray flux striking the analyzed area J, the concentration of the species of interest within the sampled volume c_a, the photoelectron cross-section α_{pc}, instrument factors K_f, and the inelastic mean free path of the electron λ_{IMFP}, according to Equation 4.7. [3]

$$I = J \times c_a \times \alpha_{pc} \times K_f \times \lambda_{IMFP} \tag{4.7}$$

As the x-ray flux remains constant, it can be ignored when comparing spectra measured with the same instrument [3]. The cross-sections α_{pc} and inelastic mean free paths λ_{IMFP} are traditionally encapsulated into relative sensitivity factors (RSF), the ratio of the photoionization cross-section with that of the C 1s orbital [3]. Species with a large RSF will be detectable at smaller concentrations than those with a small RSF, due to being more likely to emit a photoelectron under illumination [38]. RSFs are dependent on the inciting raditation [38].

RSFs are usually encompassed into the analysis software, so the only thing one needs for concentration analysis is to find the intensities of the photoelectron signals. Unfortunately, due to the effect of the inelastically scattered electron background, this is not always simple. Background subtraction routines are thus necessary to find the actual intensity of the photoelectron signal. This is one of the sections of analysis where caution is most required, as there are several different available

background types, of which the most suitable one must be chosen. [3]

4.7 XPS instrumentation

The XPS instrument is an ultrahigh vacuum instrument with several specialized components. The primary ones are the x-ray source, the extraction optics and energy filter, and the detector. The nature of electrons places additional requirements on the construction of the vacuum chambers. [3]

4.7.1 Photon source

X-rays are mostly produced with an x-ray tube. A cathode material is heated up resistively, whereupon it emits electrons, which are then guided to the anode with an electric potential. As the electrons strike the anode, they produce core holes in the anode material. These core holes relax via fluorescence, producing x-rays characteristic to the anode material. For x-ray tubes used in XPS, the most common anode materials are Aluminum (Al Kα 1486.6 eV) and Magnesium (Mg Kα 1253.6 eV). These x-rays then make their way out of the tube onto the sample. [3]

As the X-ray production is a probabilistic process, x-ray sources produce additional, rarer, peaks from K$\alpha_{3,4}$ and Kβ emission and Bremsstrahlung radiation, which may produce "ghost peaks" in the measured spectrum, or in the case of Bremsstrahlung radiation increase the level of the background signal. These can be eliminated and the energy spread of the Kα peak reduced via a monochromator. The natural energy spread is 0.85 eV for Al Kα; with a monochromator, this can be reduced to 0.4 eV. For x-ray applications the monochromator is typically a concave quartz crystal with atomic plane spacing so that Al Kα radiation at angles near 78.5° satisfies the Bragg criterion of Equation 4.8, where n is the order of diffraction, λ is the wavelength of the radiation, d is the spacing of the atomic planes, and ϕ is the angle of diffraction. [3]

$$n\lambda = 2d \sin \phi \tag{4.8}$$

The typical UPS photon source is a gas discharge lamp. Gas is pumped between an earthed cathode and an anode with a potential of c. 1 kV, which causes the electrons of the constituent atoms to excite [3]. The excited state relaxes as fluorescence [3]. The most typical gas is Helium, with He I emission at 21.2 eV and He II emission at 40.8 eV [3].

It is also possible to freely choose the energy of the inciting radiation, rather than pick the best of what nature has to offer. Synchrotrons produce radiation by forcing near–relativistic electrons onto curved paths with magnets [33]. The energy of the photons depends on the energy of the electrons [3], and is continuous from around 10 to 10^4 eV [33]. This flexibility is beneficial in analysis, and the synchrotron produces a greater intensity of photons than an x-ray tube [33]. The chief drawback of the synchrotron light source is that it requires a synchrotron, which is a significant installation [3].

4.7.2 Electrostatic lens system

The electrons emitted by the sample are gathered into an electrostatic lens system which uses electric fields to focus the stream into the analyzer. The most common analyzer in modern days is the concentric hemispherical analyzer (CHA), which consists of two hemispheres with an electric potential difference between them. As shown in Figure 4.2, electrons of the selected energy travel through to the detector; electrons with kinetic energies too high or too low hit one of the hemispheres. [3]

The selected energy range is scanned through by adjusting the acceleration/deceleration the electrons undergo in the lens system so that whatever the selected energy, electrons with that energy all arrive in the analyzer at a constant, preselected energy.

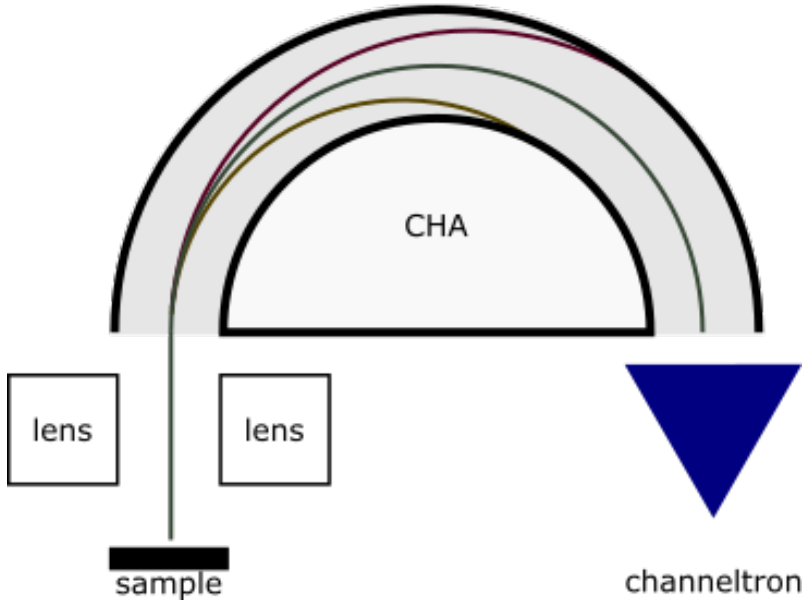

Figure 4.2 *Operation principle of the concentric hemispherical analyzer. Electrons of the selected energy travel to the detector, while electrons with too high or too low kinetic energies impact one of the hemispheres. After van der Heide [3].*

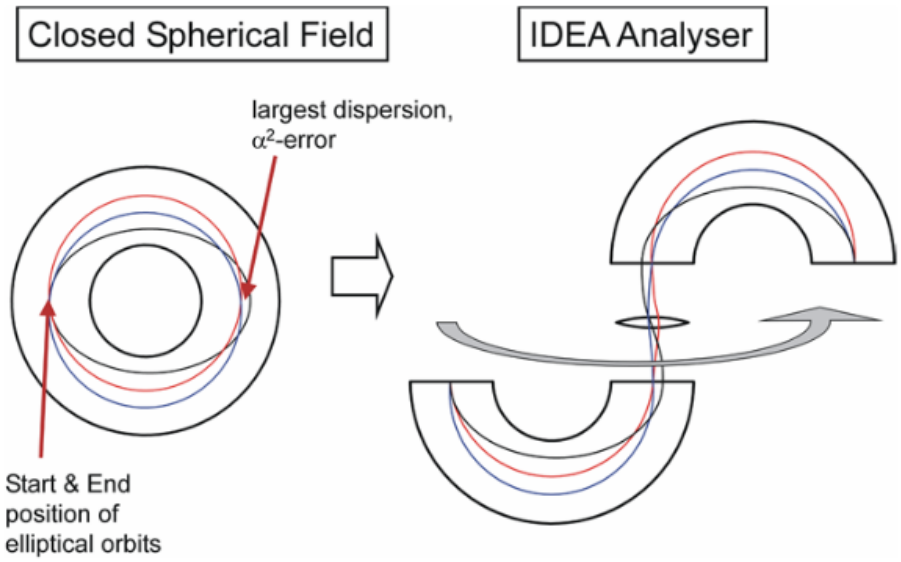

Figure 4.3 *A dual hemispherical analyzer is a means of reducing electron optical aberrations. Figure from Escher et al. [4].*

This is referred to as constant analyzer energy (CAE) mode. The energy resolution on CAE mode is constant, dependent only on the chosen energy of the analyzer, commonly referred to as pass energy. The lower the pass energy, the better the resolution, but the worse the sensitivity. [3]

The quality of the lenses of the electrostatic lens system affects the analysis area. For imaging applications, this is critical—as is the design of the analyzer. As shown in Figure 4.3, the aberration in the paths of electrons that comes from their entrance angle to the analyzer is at its highest after a half circle, i.e. at the end of the hemispherical analyzer where the detector is. FOCUS GmbH has recently come up with the novel idea of correcting for this aberration by letting the electrons travel another half "orbit", after which all electrons should be at the same location they started at. To get past the problem of how these electrons are supposed to get into the double CHA or reach the detector, the hemispheres are separated, with a transfer lens between them, as shown in Figure 4.3. [4]

4.7.3 Detector

The passage of one electron per second will generate a current of 1.602×10^{-19} A, 4 orders of magnitude beneath the current limit of detectors. As samples only rarely emit thousands of electrons per second in the energy range of interest, gain is necessary. This is typically achieved by directing the electrons into an electron multiplier, typically a tube coated with an electron-emissive material, for example

PbO. The original collected electrons hit the wall, which emits multiple electrons. These electrons then collide with the wall elsewhere and again cause multiple electron emission, causing an electron cascade that amplifies the singe-electron signal into something a detector can measure. [3]

The most common electron multiplier configurations are the channeltron and the microchannel plate (MCP). The channeltron is a horn-shaped diode with a 2 to 4 kV potential difference between the ends accelerating the electron cascade. Channeltrons exhibit gains of up to 10^8, and their chief advantage is that an array of them can be arranged onto a line, allowing simultaneous detection over a narrow energy range, or the summing of data from them to enhance sensitivity. The MCP, on the other hand, is a 2D array of capillary tubes that have been angled around 7° off the normal of the array plane. While the cascade gains are only 10^4, the MCP allows for simultaneous imaging PES. [3]

The pulses generated by the electon multiplier can be collected digitally or analogically. The analog method is the phosphor screen with an optical lens and camera gathering the incoming photon flux. This has the advantage of adding a gain of 10^8 due to one electron causing the emission of many photons. The digital method is the anode collector, which is a metal electrode connected to sensitive pulse counting electronics. A variant of the anode collector is the delay line detector, where measuring the time delay between the signal being measured at one end of the line detector and the other end of the line detector lets one calculate where along the line the signal originated from and build a 1-dimensional image. By placing a criscrossing array of two line detectors behind a MCP system, it is possible to take 2-dimensional images in real time. [3]

5. IMPEDANCE SPECTROSCOPY

Impedance spectroscopy is a relatively simple method of electrochemistry in which the impedance response of a material is measured at several frequencies of alternating current (AC). This response gives insight into the charge transport properties of the material. [39]

5.1 Principles

Many things contribute to the frequency response of a material. Atomic and electronic phenomena happen at frequencies of infrared and ultraviolet light, respectively, and are beyond the resolution capabilities of most common laboratory instruments, but dipolar and ionic phenomena are wholly observable. Impedance spectra can yield information on the dielectric properties, rates of chemical reactions, mass transport, corrosion, microstructure, defects, and compositional influences on the conductance of the sample. [39]

At the heart of all this is charge transport. The movement of electrons is the root of all current, and when electrical properties are known in the rest of the experimental setup, the properties of a sample can be found out. For materials intended for electronic or catalytic applications, charge transfer properties are important to know. [39]

5.2 Charge carrier analysis

Frequency response analysis (FRA) is a way of acquiring the impedance spectrum of the material by subjecting it to a variety of different AC frequencies and measuring the voltage between two inputs. By adding a resistor to the circuit, the impedance can be acquired. [39]

A means of extracting meaning from the measured data is to fit an equivalent circuit, which is a circuit that has the same impedance as the sample. Using resistors and capacitors to model solution resistivity, electrical double layer formation, and

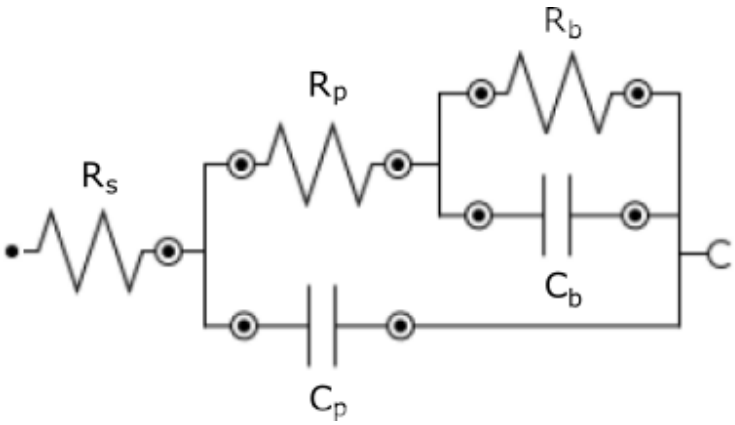

Figure 5.1 *Schematic of the circuit used to fit the FRA data. After Pan et al. [5].*

other physical phenomena present in the measurement, materials properties can be extracted. As several different forms of equivalent circuit can generate the same impedance, care must be taken when choosing the circuit, and knowledge of the sample structure and potential phenomena present is necessary. [39]

For the fitting of the impedance spectrum of a thin film that has another partial ("leaky") film on top of it, the best model is that shown in Figure 5.1. R_s is the resistance of the solution, C_p is the capacitance of the outer layer coating, R_p is the resistance of the outer layer coating, C_b is the capacitance of the inner coating layer, and R_b is the resistance of the inner coating layer. [5]

6. MATERIALS AND METHODS

6.1 ALD apparatus

A PICOSUN R-200 Advanced ALD apparatus was used to deposit the TiO_2 thin films used in this study. It is a computer–controlled system with computerized control of resistive heating, valves, carrier gas flows, and growth recipes. The reactor chamber has a constant gas flow and is pumped with an EBARA ESA70W-D Roots pump to keep it clean of impurities. Substrates are loaded via a separate loadlock that is pressurized with nitrogen to atmospheric pressures.

6.2 NanoESCA

The samples were measured with an Omicron GmbH NanoESCA system, with three vacuum chambers isolated from each other with gate valves. Samples were introduced to the system through the load lock, then left to pump overnight and brought into the preparation chamber, where the annealing was carried out. The XPS and UPS spectra were measured in the analysis chamber. Figure 6.1 shows what the analysis chamber looks like from the outside.

The analysis and preparation chambers are both pumped with their own turbomolecular pump and combined titanium sublimation and ion pump, leading to baseline pressures of around 10^{-10} mbar. The load lock is pumped from atmosphere to vacuum with a single turbomolecular pump and maintains a baseline pressure of around 10^{-8} mbar.

The analysis chamber has three photon sources: a Physical Electronics Model 36-100 Focused X-ray Source producing Al Kα x-rays, a VUV Source HIS 13 producing He I light via gas discharge, and a Hg discharge source. The x-rays are monochromated with a crystal monochromator for improved energy resolution.

A diagram of the lens system used in data acquisition is shown in Figure 6.2. The electrons are gathered from the sample into an objective lens, though which they go through a contrast aperture, octopole stigmator, an optional iris aperture, projection

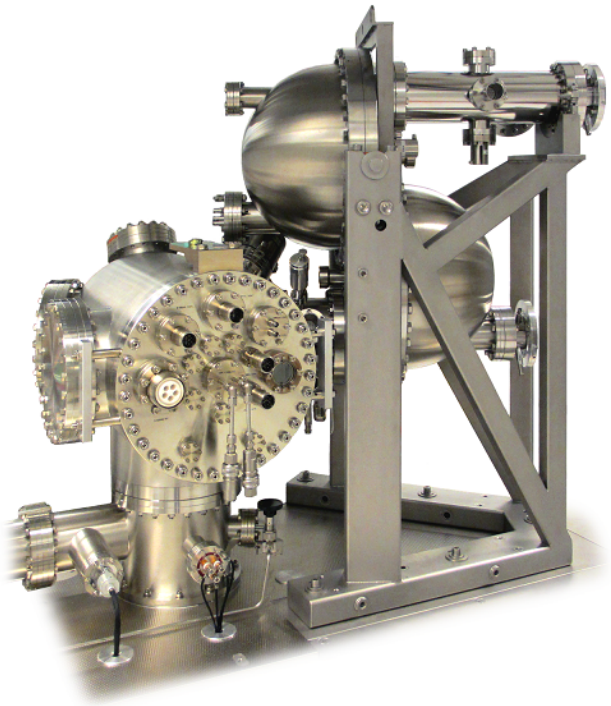

Figure 6.1 *The NanoESCA system, showcasing the double hemispherical energy analyzer and the vacuum chamber of the monochromator. Photograph by Markku Hannula.*

lenses, deflectors, and a slit into the first hemispherical energy analyzer. From there, they go through another transfer lens, and either the channeltron detector for spectral acquisition, or a second hemispherical energy analyzer and projection lenses before hitting a double MCP that amplifies the electron current. The second hemispherical analyzer compensates for the aberrations of the first hemispherical analyzer. The spatially resolved amplified electron count hits a scintillator screen made of Cerium-doped Yttrium Aluminum Garnet that emits light when hit by an electron, and this light is then turned into a digital image by observing it with a CCD.

6.3 Autolab

Photoelectrochemical measurements were made with a computer-controlled Autolab PGSTAT12 potentiostat equipped with a FRA2 module for impedance measurements (Metrohm Autolab). The control software was Nova 1.11. The samples were connected with a three-electrode connection, and measurements made in 1M NaOH solution as the electrolyte. The reference electrode was an Ag/AgCl reference electrode (Harvard Apparatus, Leak-Free reference electrode 69-0023) with 3M KCl

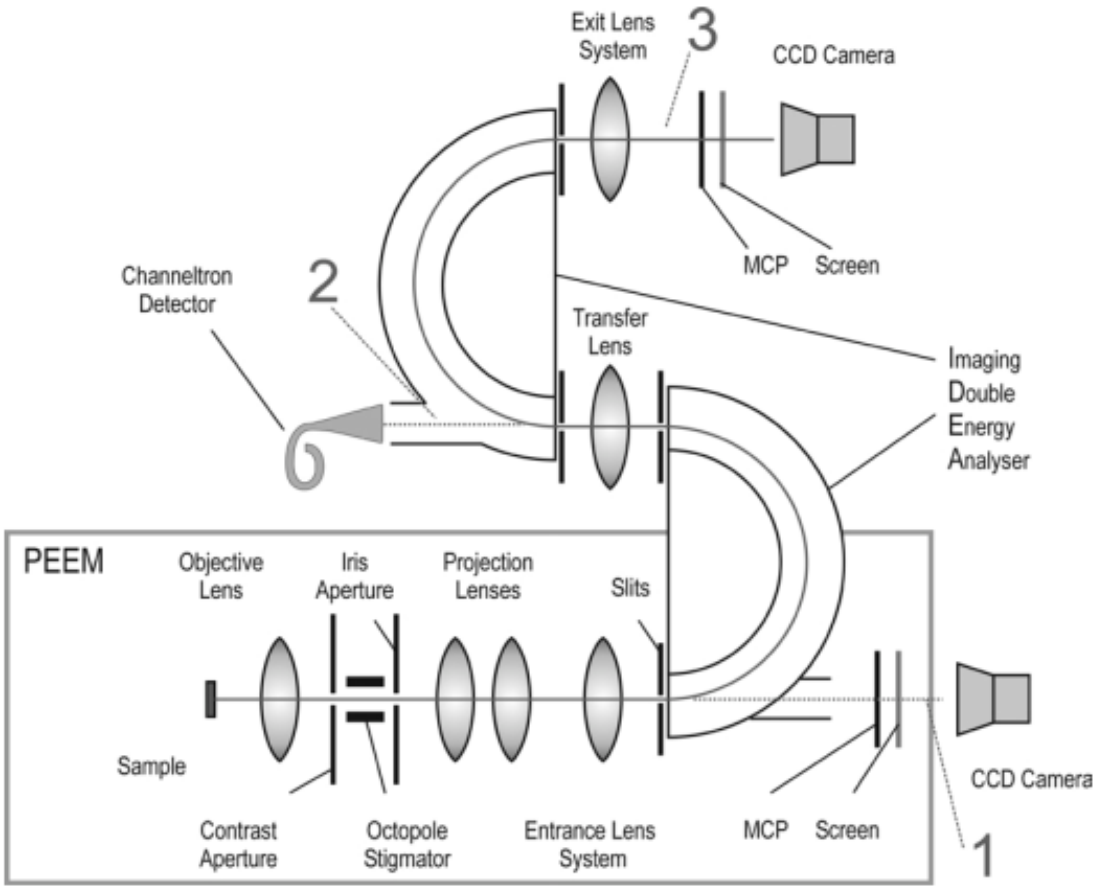

Figure 6.2 *A schematic diagram of the electron lens system of the NanoESCA. The lens system allows usage of (1) unfiltered PEEM mode (not used in this study), (2) spectroscopy, and (3) spectromicroscopy. Figure from Escher et al. [4].*

as the internal electolyte. The work electrode was the measured sample, and the counter electrode a platinum wire. Measurements were conducted in a teflon cell that exposed a controlled area of the sample to the electrolyte and the opposite wall of which was transparent glass.

6.4 Measured samples

30 nm of titanium dioxide was deposited at 200°C onto a n-Si(100)(P) substrate wafer from Wafer World, Inc. in a PICOSUN R-200 Advanced ALD reactor using tetrakis(dimethylamino)titanium and deionized water precursors. Then, nickel was lithographically deposited onto the TiO_2 surface by vaporizing metallic Ni and driving it through a mask onto the TiO_2 surface for 10 s. The mask had lines 6 µm wide with 15 µm pitch. A 2 mm by 2 mm region near the center of the mask held TUT logos 50 µm wide with 75 µm pitch. Figure 6.3, an image taken with a scanning

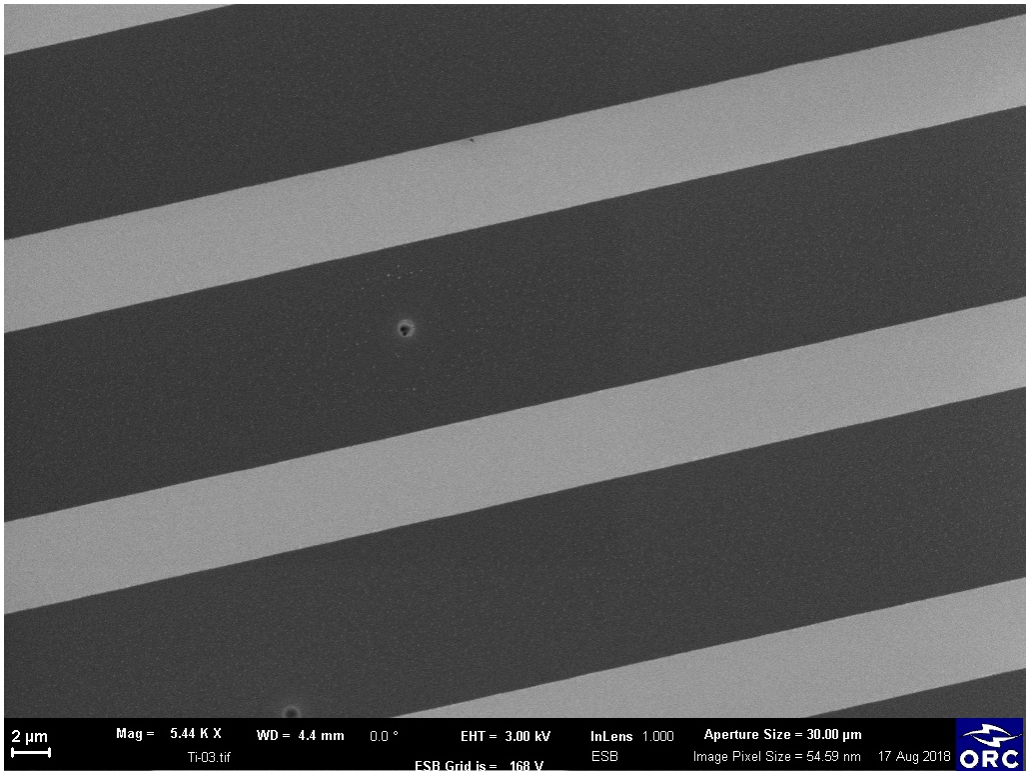

Figure 6.3 *Close-up of the Ni fingers (bright) on TiO_2, taken with a scanning electron microscope.*

electron microscope, shows that the dimensions of these lines are accurate.

A 10 mm by 10 mm sample was cleaved from the center of the wafer and loaded into the NanoESCA apparatus. Measurements were done of the as-received state and after cumulative annealing to temperatures from 400°C to 1000°C with a step of 100°C, save 600°C. Annealing was done radiatively in the preparation chamber, with the temperature measured through a viewport with a Cyclops 160B pyrometer. The emissivity of the pyrometer ϵ was 0.60, the value for the Si substrate. The value shown by the pyrometer was assumed to be the temperature of the sample. The sample was held at each temperature for 60 minutes, then left to cool, after which UPS spectra of the secondary electron tail and valence band were measured on the same day for the as-received, 400°C, 800°C, 900°C, and 1000°C samples. Later, XPS spectra were measured: a survey scan from 1350 eV to -2 eV with 200 eV pass energy in CAE mode, and detail scans of Ti 2p, Ni 2p, O 1s, C 1s and the valence band for all temperatures. A Si 2p detail scan was additionally measured for states from 700°C through 1000°C inclusive, a Fe 2p detail scan was measured for the 1000°C state, and a N 1s detail scan was measured for the as-received state. All detail scans were measured with pass energy 100 eV in CAE mode.

The fittings for Ti, O, C, N, and Si were done according to Hannula *et al.* [40]. Ni fittings were done after Herrera-Gomez *et al.* [41] for metallic Ni^0 and after Biesinger *et al.* [34] for NiO, using several Gaussian-Lorentzian peaks to construct an accurate lineshape. Fe was fitted with a single Gaussian-Lorentzian peak. The spectra were not corrected for the transmission function, as the transmission function of the NanoESCA instrument is approximately constant for KE above c. 600 eV, and the photoelectrons of all spectral lines used for quantification have kinetic energies above that.

A FRA measurement was made for an as-received sample and samples cumulatively annealed to 400°C and 800°C. Using Nova 1.11 software, an equivalent circuit of R(C[R(CR)]) form—displayed in Figure 5.1—was used to fit the data.

6.5 Image analysis

Images were measured with both x-ray and UV radiation sources. All images had the background subtracted with a Matlab script that averaged the values at 20 times 20 pixel squares at the corners of the image (nominally black due to the electron image being circular), then subtracted that value from all pixels, and finally set the intensity levels of all pixels outside of the circular image area to zero. After this, the resulting image stack was opened in ImageJ and outlying bright pixels were removed.

For x-ray core level images, that image sequence was converted into a Vamas file using the Focus NanoESCA measurement software and opened with CasaXPS. In CasaXPS, the spectra from each pixel were summed, then elemental components fit to the sum spectra and propagated back to the spectra at pixels. These were combined back into chemical composition maps.

To compare the Ni fingers with regions between the fingers, the background-subtracted image stack with outliers removed was opened in ImageJ, and z-profiles taken from an area on the finger closest to the image center and an area between the fingers. These were imported into CasaXPS as spectra and components fitted to them. Due to the decreased energy resolution of images compared to channeltron spectra, speciation from images is less precise, and Ti^{2+} could not be resolved.

For the UPS images, after the removal of outliers, the images had the parabolic energy dispersion corrected with an equivalently-measured image from a flat n-Si(111) sample. The images from the flat n-Si(111) had their background subtracted with the same script and bright outliers removed with ImageJ, after which the work

function was calculated with 31px by 31px smoothing to map out the parabolic energy dispersion. The work function was calculated with a Matlab script that fitted straight lines to the secondary electron cutoff and the slope leading to it; the secondary electron cutoff ($E_K - E_F$) is the work function, assuming that the Fermi energy is at 0 eV (BE). With the assumption that the apex of the parabola was at the correct energy, the images of the Ni/TiO_2 were energy corrected. After this, the work function was calculated from the corrected images. 0.098 eV was added to this calculated value to account for the Schottky effect caused by the accelerating electric field [35] and acquire the final result.

7. RESULTS AND DISCUSSION

The atomic concentrations of elements present in the sample at the selected annealing temperatures are gathered into Table 7.1. 7 at-% of C was present as a surface impurity; this may be either atmospheric contamination or remnants of incompletely dissociated ALD precursors. The Ni fingers and the interfinger zones had a clearly defined difference in work function, though because the amount of atmospheric contaminants may be different in different regions, no absolute value for the work function of the as-received TiO_2 or Ni fingers work function can be given. As seen in Figure 7.1, in the as-received state, the Ti in the sample was mainly Ti^{4+}, though about a quarter of the signal came from Ti^{3+} due to the fact that ALD produces a nonstoichiometric film that has oxygen vacancies. Fitting spectral components for both NiO and metallic Ni showed the Ni to be oxide, corroborated by the valence band spectrum (Figure 7.2) showing a lack of density of states near the Fermi edge.

Table 7.1 *Elemental concentrations in at-% for the Ni-fingers/TiO_2/n-Si sample as a function of annealing temperature.*

Temperature / °C	Ti	Ni	O	C	Si	Fe
as-received	22.3	5.3	65.4	7.0		
400	27.3	3.4	65.0	4.1		
500	27.0	3.2	66.3	3.6		
700	28.3	1.7	69.1	0.6	0.3	
800	27.0	0.1	70.8	0.2	1.9	
900	29.2	0	69.5	0.3	1.0	
1000	6.1	0.9	1.2		91.6	0.1

At 400°C, the secondary electron images and work function image (Figure 7.3) both show that while the Ni fingers still remain, they and the space between them have become slightly mottled. In the core-level images no such phenomenon is noticeable, so likely the changes in work function are related to the reduction of Ti, rather than surface diffusion of Ni. As can be seen in Figure 7.2, the Ni 2p signal shows that the Ni has reduced from its native oxide to metallic Ni^0, which is also reflected in the XPS valence spectrum showing significant density of states at the Fermi edge, indicative of metallic species present on the surface. The work function of the stripes,

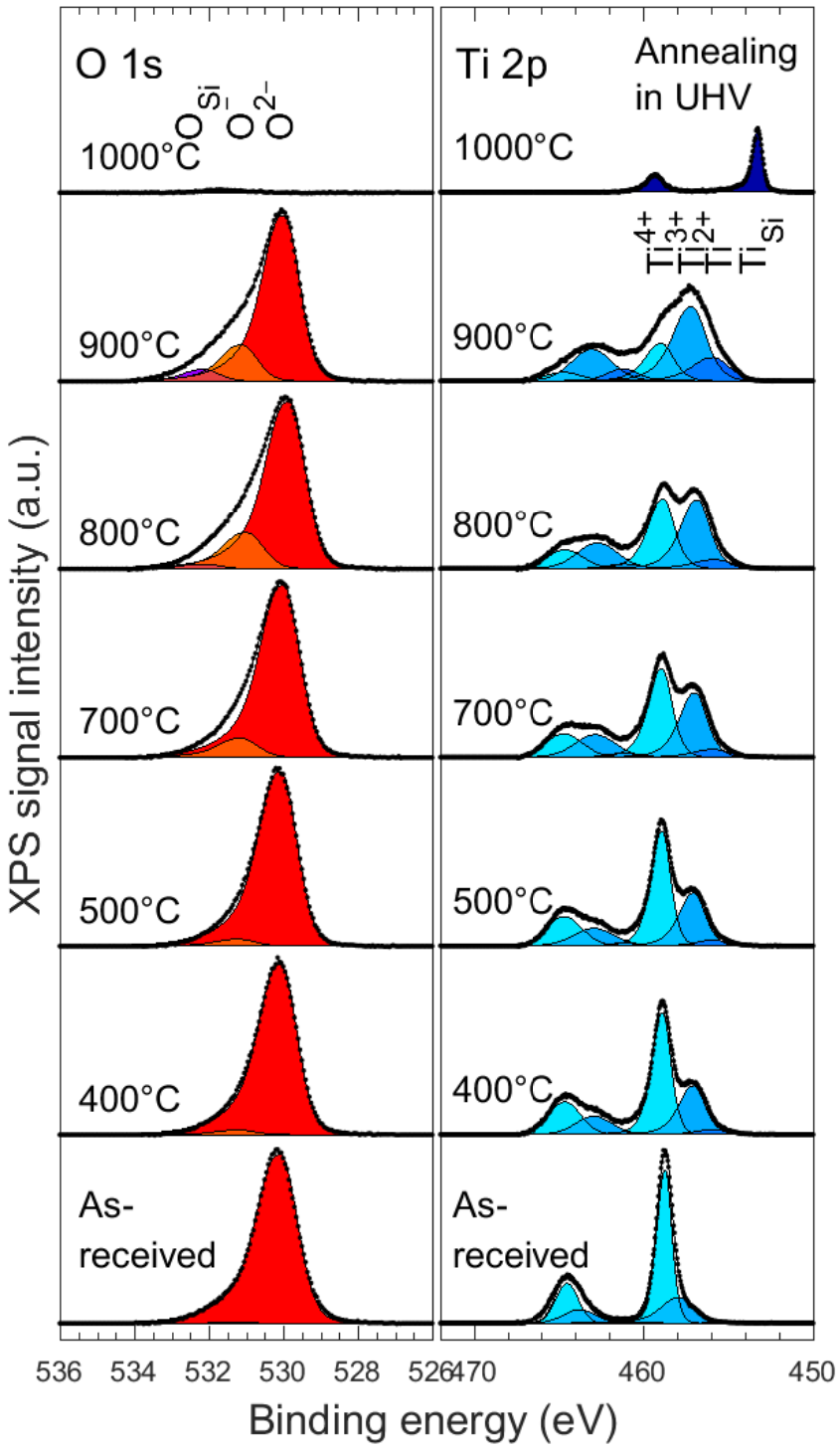

Figure 7.1 *Evolution of O 1s (left) and Ti 2p (right) peaks from the as-received state to the 1000° C annealed state. The sum envelope is drawn in black and the fitted components in shades of red (O 1s) or blue (Ti 2p). For Ti 2p, both Ti $2p_{3/2}$ and Ti $2p_{1/2}$ peaks are fitted, with four synthetic components in each spin–orbit coupled state.*

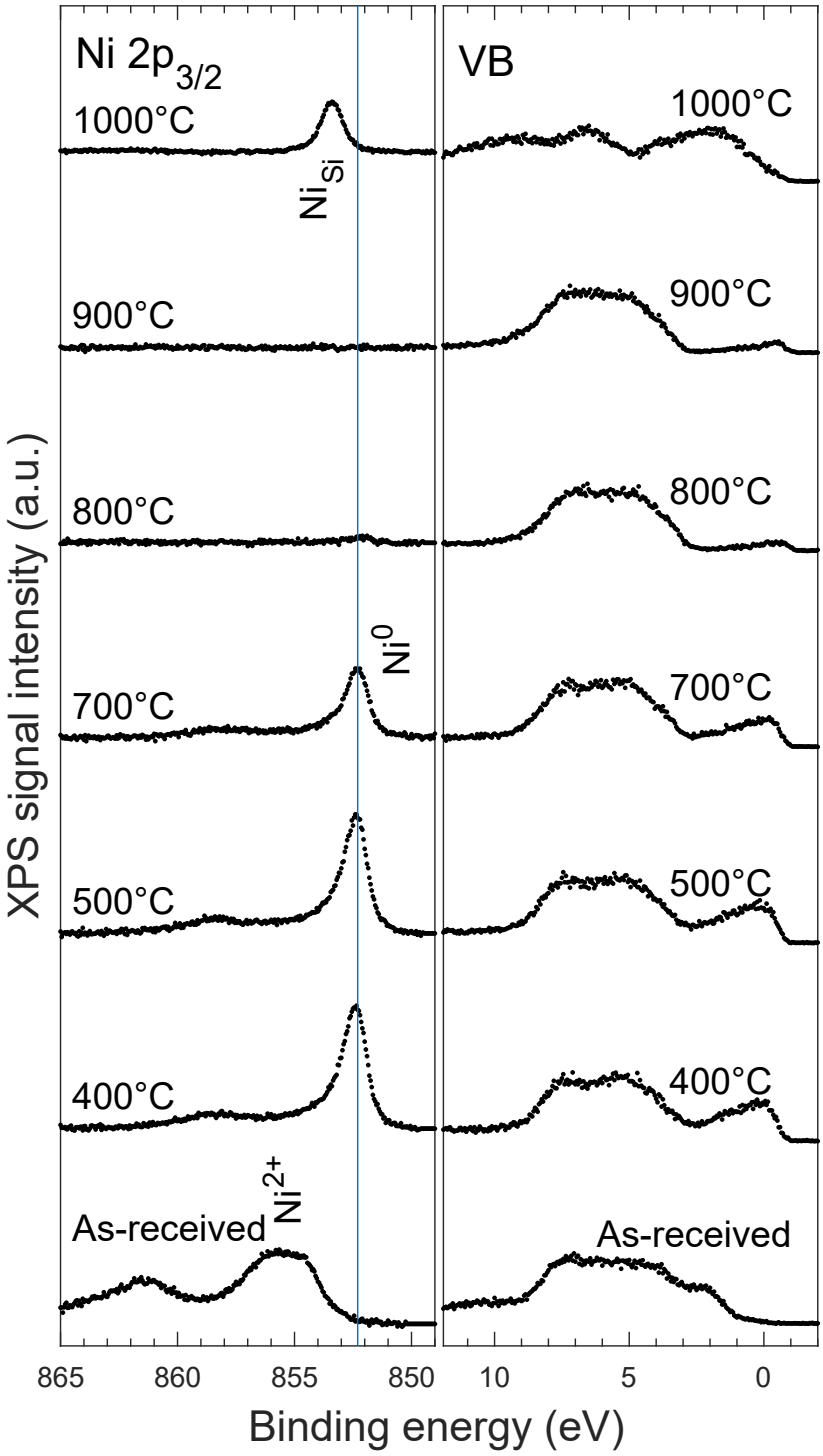

Figure 7.2 *Evolution of Ni $2p_{3/2}$ (left) and valence band (right) peaks from the as-received state to the 1000° C annealed state. The feature at higher binding energies to the main peak is the shake-up feature. The presence of metallic Ni is visible in the valence band density of states at the Fermi edge.*

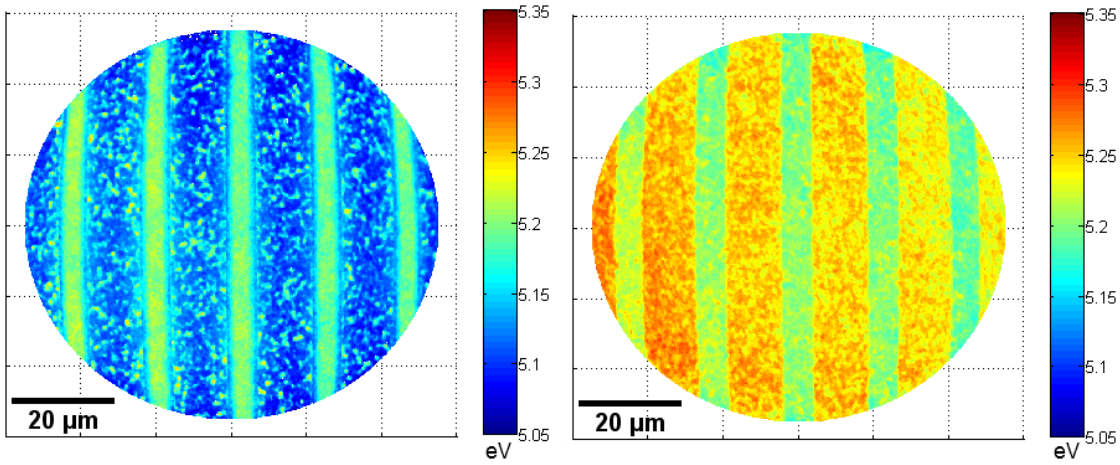

Figure 7.3 *Work functions of 400° C (left) and 800° C (right) surfaces. The energy scale is the same in both images, revealing that the work function of the Ni fingers remains constant while the work function of the surrounding TiO_2 changes.*

5.2 eV, is also similar to the work function of metallic Ni, 5.15 eV [42]. The 500°C case has similar shapes and intensities of Ni, O, C, and valence signal as at 400°C, with the only change being an increase in Ti suboxides.

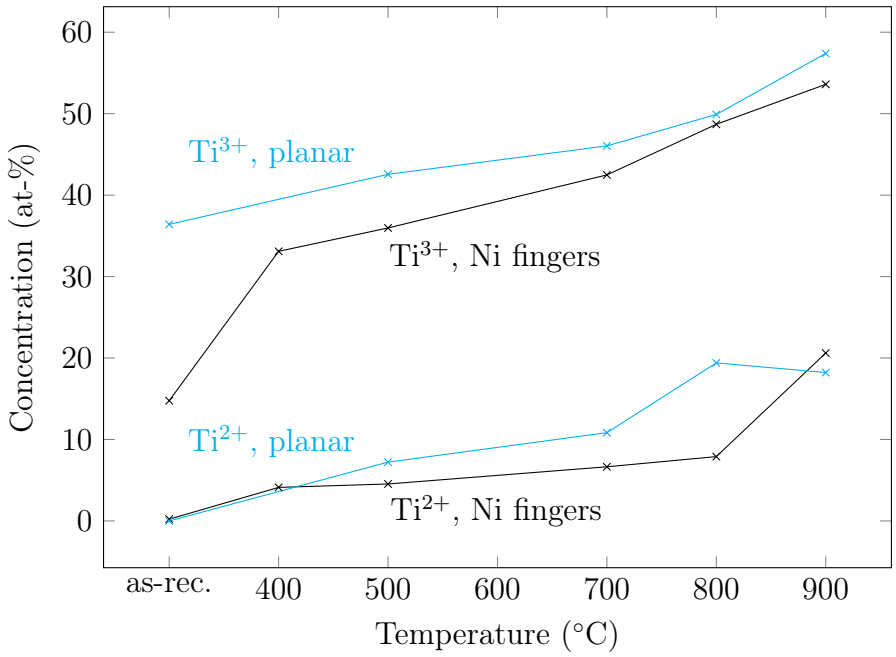

Figure 7.4 *Reduction of Ti in Ni fingers/TiO_2 (large area average) and planar TiO_2 reference as measured by the percentage of Ti signal that is Ti^{2+} or Ti^{3+}. The remaining fraction is of Ti^{4+}. At 1000° C, the samples are Ti_{Si} in silicide. The 400° C case was not measured for the planar TiO_2.*

Table 7.2 *$Ti^{3+/2+}$ as a percentage of Ti 2p signal between the fingers and beneath them at selected temperatures. Only two components were fitted, $Ti^{3+/2+}$ and Ti^{4+}.*

Temperature / °C	Between fingers / %	At fingers / %
as-received	19	15
400	40	31
800	66	63
900	72	71

At 700°C the Ni signal has begun to attenuate. A shoulder has appeared on the higher binding energy side of the O 1s peak in Figure 7.1 due to the increased amount of undercoordinated O that is bonded to Ti suboxides, identifiable as O^-. The amount of residual carbon has gone down. The Si 2p signal is observable, though minute. The most visible change, however, is the further reduction of Ti.

At 800°C, the Ni has almost completely disappeared from the surface. Its influence still shows, however, in the work function (Figure 7.3) and in the oxidation state of the Ti (Table 7.2). Where there once were Ni stripes, the Ti is less reduced, and the work function at the stripes remains the same as at 400°C. Between the stripes, the work function of the TiO_x increased above that of the Ni, from 5.1 eV to 5.25 eV. The comparison between the 400°C and 800°C work functions is in Figure 7.3. The Si concentration on the surface has grown, which is also reflected in the O 1s peak acquiring an O_{Si} component (Figure 7.1).

At 900°C, the shoulder of the O 1s peak continues to grow, seen in Figure 7.1. The

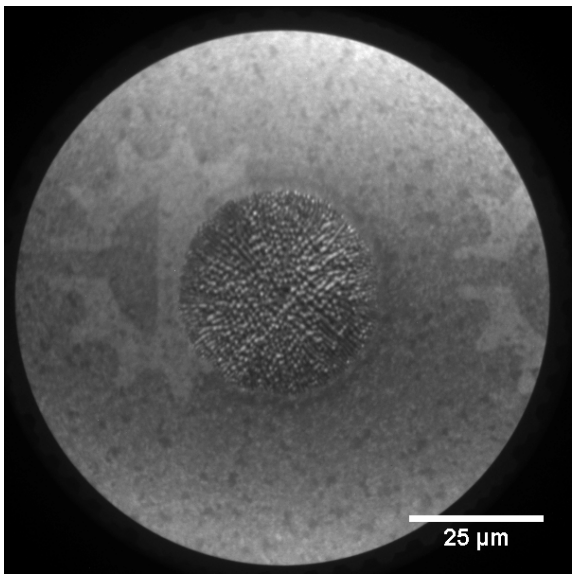

Figure 7.5 *Crater and mottling near 50 µm diameter TUT logos after 900° C annealing. Image taken at E_K =5.1 eV.*

Si 2p signal decreases temporarily, and the Ni signal is beneath the detection limit. Most of the Ti is now Ti^{3+}, with a significant Ti^{2+} contribution appearing, seen in Figure 7.4. The work function has increased, though the remnants of the Ni stripes are still visible as regions with lower work function (5.7 eV vs. 5.8 eV, displayed in Table 7.3). On the Ni-TiO_2 surface, cratering indicative of TiSi formation beginning was already visible after 60 min at 900°C, as seen in Figure 7.5. For unpatterned TiO_2, a similar situation is produced by annealing for 10 minutes at 930–940°C [43].

When the temperature is increased to 1000°C, the surface has wholly restructured from TiO_x into silicide, with the Ti now Ti_{Si} and the O 1s signal dramatically decreased, as shown in Figure 7.1. The Si 2p peak, in Figure 7.6, is split between TiSi and elemental Si. The work function shows no variation beyond the minor

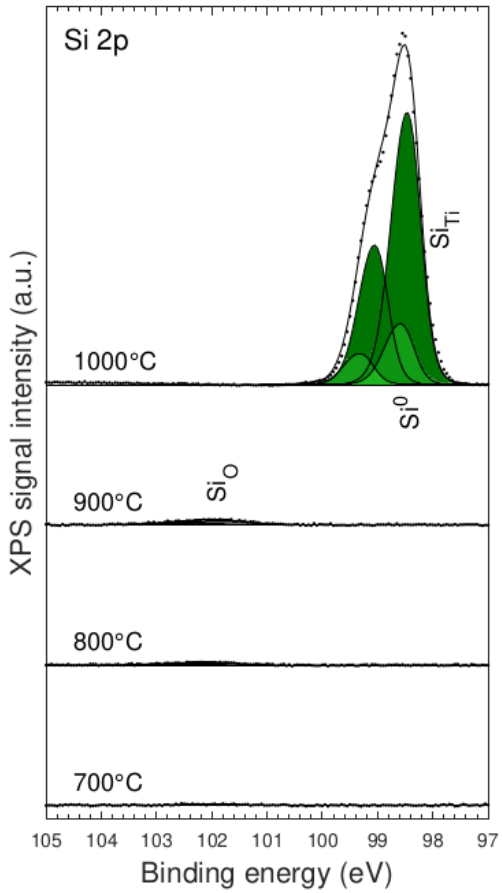

Figure 7.6 *Evolution of Si 2p from the 700° C annealed state to the 1000° C annealed state. Beneath 1000° C, the peak is SiO_x. At 1000° C, it is elemental Si and silicide. Both Si $2p_{3/2}$ and Si $2p_{1/2}$ peaks are fitted, with three synthetic components in each spin–orbit coupled state.*

effects of the surface morphology. The work function value, found in Table 7.3, is 4.75 eV; for elemental Si, it is 4.85 eV [42]. Fe and Ni are also present, as they segregate from the wafer towards the surface. No lateral contrast was observable. With XPS, it is impossible to distinguish between Ni that was originally in the Ni fingers before diffusing into the bulk Si and back and Ni that originated as an impurity in the Si wafer. The Fe $2p_{3/2}$ peak is at 706.6 eV, which fits both metallic Fe [34] and $Fe_{0.7}Ni_{0.3}$ [44].

7.1 Ti reduction

Compared to a planar TiO_2/Si sample deposited with the same deposition parameters and cumulatively annealed for 30 min for each temperature, measured at an earlier date by Markku Hannula, the Ti in the Ni-TiO_2 sample reduces somewhat slower, despite the longer 60 min treatment time. The percentage of Ti^{3+} and Ti^{2+} in channeltron data is illustrated in Figure 7.4. The 400°C case was not measured for the planar TiO_2. At 1000°C, the Ti had reduced to Ti_{Si} and formed silicide for both samples. For the finger sample, the progression of the O and Ti signals and the decrease in Ti^{4+} and growth in Ti suboxides and O^- as the annealing temperature is increased up to 900°C can be seen in Figure 7.1.

When comparing the Ti signal from beneath and between the Ni fingers, it is noticeable that the Ti reduces much more between the fingers than beneath them. As this is accompanied by a reduction of the Ni, it is clear that the Ni reduces preferentially. The percentages of Ti which are $Ti^{3+/2+}$ in selected regions of the Ti 2p image are gathered into Table 7.2. As the energy resolution of the spectromicroscopy results was not enough to distinguish Ti^{2+} from Ti^{3+}, only one peak was fitted for the suboxide state.

7.2 Ni behavior

The Ni is in its native oxide form after lithography, and reduces at 400°C to metallic Ni, as evidenced by both core-level Ni 2p spectra and the valence band acquiring density of states near the Fermi edge. The spectral data for selected temperatures is shown in Figure 7.2. As-received, it was wholly oxidized, and at 400°C was 81% metallic, further reducing to 87% metallic at 700°C. Above 700°C, the Ni signal disappeared, so that at 800°C it was only barely distinguishable and at 900°C it was nonexistent. At 1000°C, the Ni from the substrate diffuses back onto the surface, though it is impossible to tell the origin of this Ni—Ni fingers or impurities in the

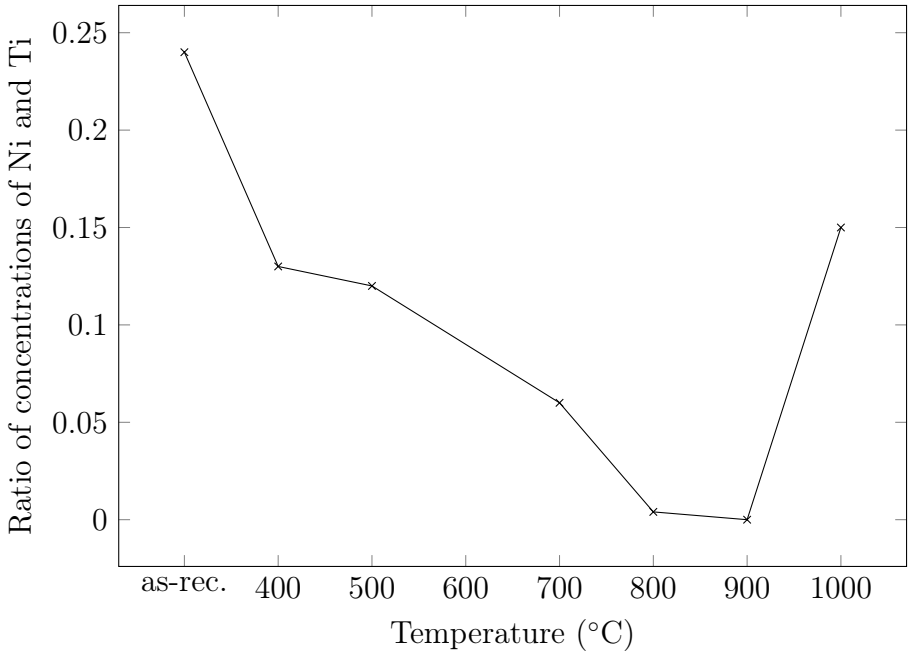

Figure 7.7 *Diffusion of Ni in Ni fingers/TiO_2/n-Si, as measured by the ratio of Ni concentration to the concentration of Ti, $\frac{c_{Ni}}{c_{Ti}}$.*

Si—from chemical state or otherwise. Its peak is at 853.4 eV, which fits well with the value Cao *et al.* have given for Ni_2Si [45]. From 400°C to 700°C, the Ni peak is at 852.3 eV.

The presence of metallic Ni is also visible in the XPS valence band spectra. In the as-received state, the valence band has little density near the Fermi edge, as showcased in Figure 7.2. Annealing to 400°C brings a separate peak of density of states to the Fermi edge, indicating presence of metallic species; continued annealing decreases its intensity, but keeps the shape. At 1000°C, the band changes shape again due to the TiO_2 surface reconstructing into TiNiSi.

The diffusion of Ni from the surface can be readily observed in the Ni/Ti ratio, plotted in Figure 7.7, as well as the decrease in valence band density of states. The reduction of the ratio indicates that the Ni diffuses into the TiO_2 film and the n-Si below, before segregating back to the surface.

7.3 Work function

Values for work function have also been gathered into Table 7.3. There and in the work function images in Figure 7.3 it can be clearly seen that the work function of the Ni stays the same between 400°C and 800°C, with only the work function of the

surrounding TiO_x changing with its changing oxidation state.

Table 7.3 *Work function in eV at and between Ni fingers, as determined from work function images, rounded to the nearest 0.05 eV.*

Temperature / °C	Between fingers / eV	At fingers / eV
as-received	5.75	5.60
400	5.10	5.20
800	5.25	5.20
900	5.80	5.65
1000	4.75	

An exciting thing to observe is the 900°C value. There is little to no Ni present on the surface, but a difference in work function values is still clearly observable. It is possible to change the work function via doping [46], so the work function of the finger regions might represent Ni-doped TiO_2.

Using the formula given by Novikov [46] for calculating the change in work function, $E_F = E_{F,i} + k_B T \ln \Omega$, where E_F is the measured Fermi energy, $E_{F,i}$ the intrinsic Fermi energy, k_B the Boltzmann constant, T the temperature in Kelvin (here room temperature of 20°C), and Ω the doping factor $\sqrt{\frac{p_b}{n_b}} = \frac{p_b}{p_i} = \frac{n_i}{n_b}$, it is possible to calculate the excess charge carrier concentration. Using Equation 4.5, we can see that if the vacuum level E_v remains constant, $E_F - E_{F,i} = \Phi_i - \Phi = k_B T \ln \Omega$. For the 900°C sample, with the assumption that the value between the fingers is the intrinsic value, inserting the measured values would result in a doping factor $\Omega = 380$.

Comparing to literature, the 5.2 eV value for the Ni fingers at 400°C and 800°C is similar to the value for metallic Ni, 5.15 eV [42]. The 1000°C value, 4.75 eV, is smaller than the values for elemental Si, 4.85 eV [42], or Ni_2Si, 4.96 eV [45]. A TiSi sample measured earlier with the same system had a work function of 4.4 eV [43]. That the work function is intermediate to those of TiSi and Ni_2Si suggests that the 1000°C surface is TiNiSi.

7.4 PEC results

The impedance spectra were iteratively fitted with the two time constant circuit described in Figure 5.1 using the NOVA 1.11 program. The values acquired for the various components are gathered to Table 7.4. The capacitance of the outer layer, C_b, increases, which is consistent with the outer layer of Ni diminishing. While the model circuit fits the as-received and 400°C samples adequately, for the 800°C

sample a third time constant appears for medium frequencies, between 100 and 1000 Hz.

Impedance data, shown in Figure 7.9, also shows that the charge transfer grows easier with increasing annealing temperature. This is likely due to the diffusion of Ni through the TiO_2 into the Si substrate. The substrate is n-Si doped with P, and P forms P^+ ions that are donor states [20]. When Ni is used to dope Si, it forms Ni^- ions that accept an electron from the bulk Si, creating a hole [20]. It can be inferred that as the Ni atoms that have first reduced from their oxidised state diffuse into the bulk, they add to the free charge carrier concentration, as evidenced by the decrease in R_p, and change the majority charge carrier type.

Chopped light constant potential amperometry (CA) data is shown in Figure 7.8.

Table 7.4 *Values of circuit components from data fitted with the circuit of Figure 5.1.*

Circuit element	as received	400°C	800°C
R_s	0 Ω	28.6 Ω	110 Ω
C_p	8.38 nF	7.98 nF	3.56 nF
R_p	25.6 kΩ	4.96 kΩ	2.25 kΩ
C_b	3.57 µF	7.75 µF	7.89 µF
R_b	2.73 MΩ	582 kΩ	932 kΩ

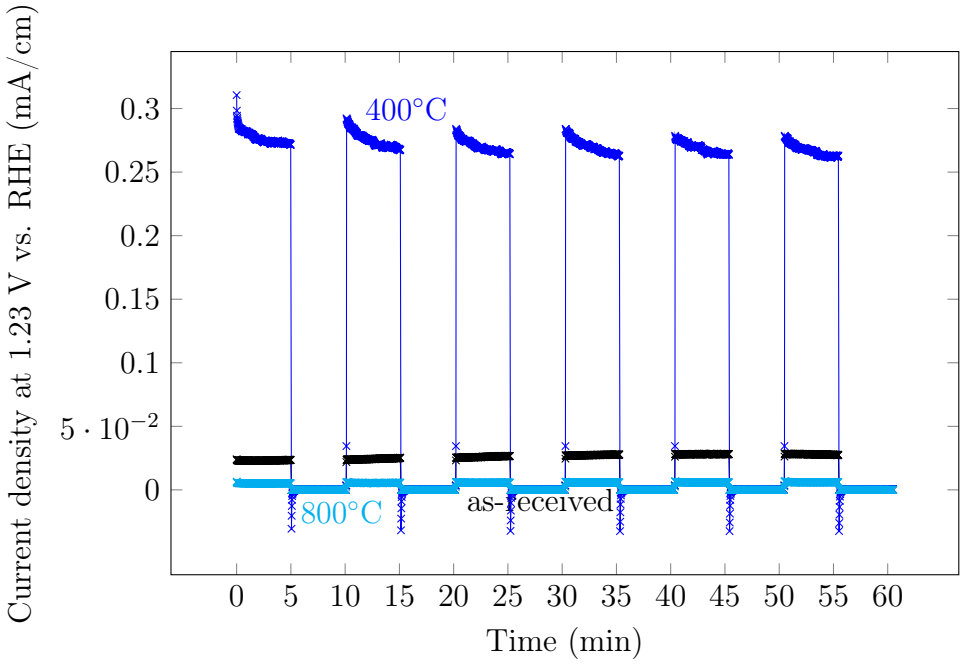

Figure 7.8 *Chopped light constant potential amperometry of the three electrochemically measured samples. The 400° C case (blue) exhibits a dramatic increase in photocurrent compared to the as-received state (black). The 800° C case (cyan) is less impressive.*

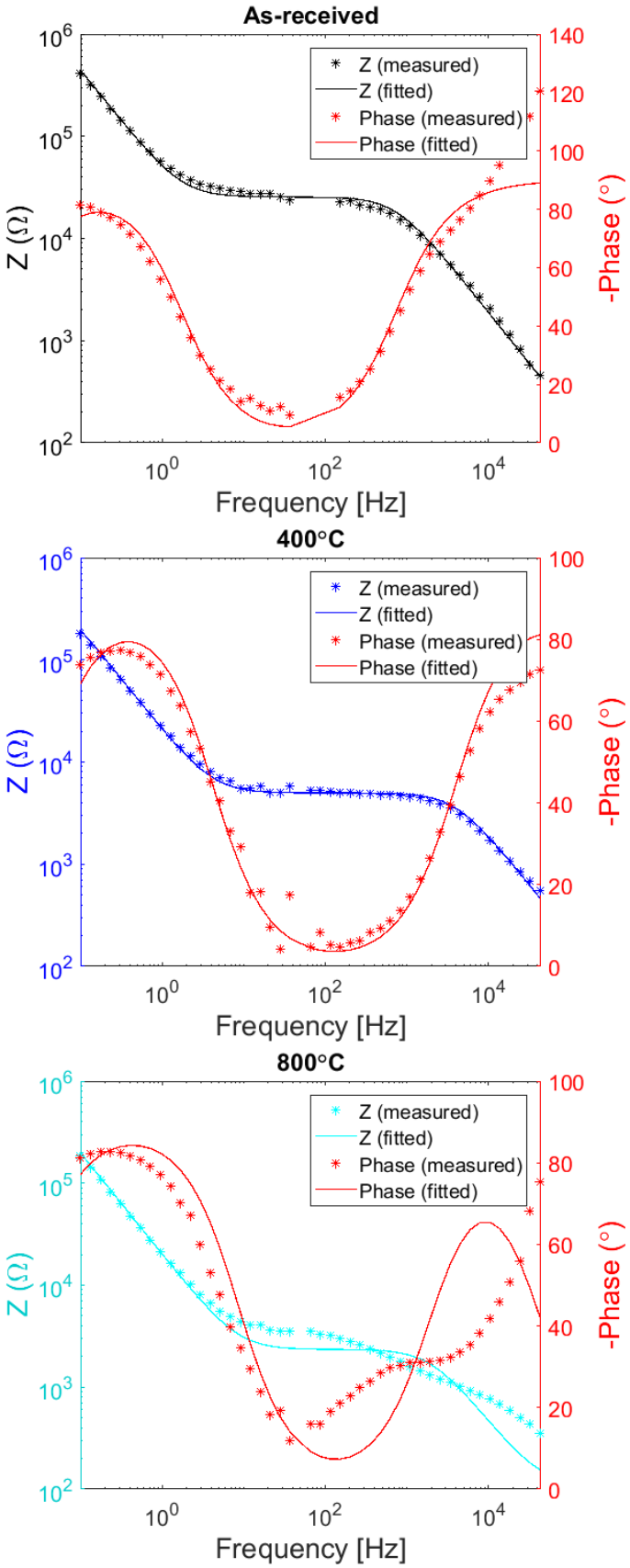

Figure 7.9 *Comparison of raw and fitted impedance data for the three samples. Top: as-received. Center: 400° C. Bottom: 800° C. Asterisks indicate the measured data and solid lines the simulated fit. Note the new time constant that has appeared at 800° C.*

The 400°C sample shows a dramatic increase in photocurrent and stability when compared to the as-received sample. This increase is likely due to the Ni reducing from its native oxide to Ni^0 and diffusing into the TiO_2 to act as a more efficient charge carrier. Under the measurement circumstances, Ni oxidizes to NiO, so the 400°C sample is likely TiO_2 with a NiO cocatalyst, which is an excellent catalyst for total water splitting [16]. Diffused Ni in the TiO_2 layer will act as a charge diffusion pathway from the surface to the Si substrate, improving water splitting by improving charge carrier transport, much like in the Ni/SiO_2/n-Si system described by Zhao *et al.* [24].

At 800°C, the photocurrent reduces drastically, likely due to the Ni reaching the Si substrate, increasing its conductivity but forming Ni/Si interface states that are unwanted for photocatalysis [7] and SiO_x barrier oxide formation at the TiO_2/Si interface. An intermediate SiO_x layer would add another time constant to the system, as witnessed in the impedance spectroscopy in Figure 7.9. The lack of Ni at the surface would mean that less of it is available for catalysis, and the increased concentration of Ti suboxides both make TiO_2 a worse photocatalyst [40] and might interfere with charge transport through the TiO_2 film due to increased amount of recombination centers [18].

7.5 Implications of results to future water splitting research

As the sample is reduced, the Ni diffuses into the TiO_2 thinfilm and the n-Si bulk. On the way, it forms a structure where there is surface Ni as a cocatalyst, as well as Ni tendrils in an amorphous oxide film that protects the n-Si from corrosion, like in the Ni/SiO_2/n-Si system described by Zhao *et al.* [24]. The Ti suboxides in the TiO_2 thinfilm form a continuum of intergap states through which electrons can be transported [7, 14], and the Ni augments this conductivity.

With further reduction, the Ni diffuses away from the surface and is not present to cocatalyze solar water splitting. Additionally, increased defects lead to charge carrier recombination, and the reaction of O present in the TiO_2 film with the Si substrate will lead to the formation of an insulating SiO_x interface.

The comparison of these results to the investigation of amorphous TiO_2 by Hu *et al.* [7] gives insight into one potential avenue of further improvement. It is likely that the deposition technique of Ni would affect the photocatalytic properties of the sample, as techniques that might locally warm up the surface would promote diffusion of Ni into the protective layer of amorphous TiO_2. Intriguingly, other research where TiO_2 films were annealed in air at moderate temperatures (400–500°C) after deposition

of TiO_2 but before Ni deposition showed that the crystallinity of the films did not affect the photocurrent, provided the films were thick enough [47]. This is likely due to the electronic structure of crystalline and amorphous TiO_2 being similar [14]. As the Ni deposition method McDowell *et al.* [47] used was radiofrequency magnetron sputtering, it is possible that the temperature of the surface was high enough to diffuse Ni into the TiO_2 film and increase charge transport.

8. CONCLUSIONS

Solar water splitting is a potential means of saving the planet with renewable energy. Gathering the hydrogen split from water and storing it for later use would be a major success, as the chemical potential of a stored quantity of hydrogen does not decay as fast as that of a battery. While economical solar water splitting is as of yet an unreached holy grail, one promising means of reaching this goal is adding a cocatalyst to the main photocatalyst. In this thesis, the cocatalyst–photocatalyst pair investigated was Ni on amorphous TiO_2 protecting n-Si, all of which are Earth–abundant and environmentally nontoxic. As another means of improving the solar hydrogen yield of n-Si is protecting it with Ni-decorated porous SiO_2, where the Ni is present both as a cocatalyst and an aid in charge transfer through the protective oxide layer, the reduction behavior of Ni was investigated during vacuum annealing to see whether Ni would diffuse into TiO_2 and produce better photocurrent.

ALD was used to deposit 30 nm of TiO_2 on n-Si(100)(P) at 200°C. A finger pattern of Ni was photolithographically deposited for 10 s on the am-TiO_2/n-Si(100)(P) substrate, after which a sample was cumulatively annealed in UHV conditions and investigated with photoelectron spectroscopy. Separate samples were prepared for photoelectrochemical measurements, with the selected data points being the as-received state, the 400°C anneal, and the cumulative 800°C anneal.

The measured data clearly show that the Ni reduces first, protecting the TiO_2 from reduction. Only after the Ni has reduced to Ni^0 does the formation of Ti suboxides Ti^{3+} and Ti^{2+} start, and then first between the fingers. At 400°C and increasingly above 500°C, the Ni slowly starts to diffuse into the bulk so that its signal is undetectable at 900°C and almost so at 800°C. The concentration of Ti suboxides, Ti^{3+} and Ti^{2+}, increases with the increased annealing temperature. This shows also in the electrochemical data, where at 800°C the photocurrent is much lesser than even in the as-received state, due to the lack of Ni species on the surface. The as-received sample has only marginally better photocurrent. The best photocurrent was found in the 400°C sample, due to Ni diffusing into the TiO_2 film to aid in charge transfer. At PEC conditions, Ni has oxidized to NiO, so the catalyst species present on the surface was NiO.

In coming times, a comparison of different materials processing parameters could yield knowledge on how to further improve solar to hydrogen efficiency. On the photoelectrochemical side, comparison of a planar film of Ni atop TiO_2 and the patterned situation measured here should be a productive avenue of investigation, as would comparison of Ni to Pt or Ir cocatalysts equivalently deposited. In the realm of PES, comparing these results to those of equivalent samples with a different means of Ni deposition would be interesting, as would be doing a depth profile of the diffused Ni or investigating the effect of the titanium dioxide on the reduction behavior of the Ni and the TiO_2 by doing an equivalent study with TiO_2 deposited at another temperature.

BIBLIOGRAPHY

[1] T. Kääriäinen, D. Cameron, M. Kääriäinen, and A. Sherman, *Atomic Layer Deposition: Principles, Characteristics, and Nanotechnology Applications*, 2nd ed. Hoboken, NJ, USA: John Wiley & Sons, Inc., May 2013.

[2] M. P. Seah and W. A. Dench, "Quantitative electron spectroscopy of surfaces: A standard data base for electron inelastic mean free paths in solids," *Surface and Interface Analysis*, vol. 1, no. 1, pp. 2–11, 1979.

[3] P. van der Heide, *X-Ray Photoeloectron Spectroscopy: An Introduction to Principles and Practices*. John Wiley & Sons, 2012.

[4] M. Escher, N. Weber, M. Merkel, C. Ziethen, P. Bernhard, G. Schönhense, S. Schmidt, F. Forster, F. Reinert, B. Krömker, and D. Funnemann, "Nanoelectron spectroscopy for chemical analysis: a novel energy filter for imaging x-ray photoemission spectroscopy," *Journal of Physics: Condensed Matter*, vol. 17, no. 16, pp. S1329–S1338, Apr. 2005. [Online]. Available: http://stacks.iop.org/0953-8984/17/i=16/a=004?key=crossref.7404af363670c6267cb91053b0f1bf74

[5] J. Pan, D. Thierry, and C. Leygraf, "Electrochemical impedance spectroscopy study of the passive oxide film on titanium for implant application," *Electrochimica Acta*, vol. 41, no. 7-8, pp. 1143–1153, May 1996. [Online]. Available: http://linkinghub.elsevier.com/retrieve/pii/0013468695004653

[6] M. G. Walter, E. L. Warren, J. R. McKone, S. W. Boettcher, Q. Mi, E. A. Santori, and N. S. Lewis, "Solar Water Splitting Cells," *Chemical Reviews*, vol. 110, no. 11, pp. 6446–6473, Nov. 2010. [Online]. Available: http://pubs.acs.org/doi/abs/10.1021/cr1002326

[7] S. Hu, M. R. Shaner, J. A. Beardslee, M. Lichterman, B. S. Brunschwig, and N. S. Lewis, "Amorphous TiO_2 coatings stabilize Si, GaAs, and GaP photoanodes for efficient water oxidation," *Science*, vol. 344, no. 6187, pp. 1005–1009, May 2014. [Online]. Available: http://www.sciencemag.org/cgi/doi/10.1126/science.1251428

[8] K. Domen, A. Kudo, T. Onishi, N. Kosugi, and H. Kuroda, "Photocatalytic decomposition of water into hydrogen and oxygen over nickel(II) oxide-strontium titanate ($SrTiO_3$) powder. 1. Structure of the catalysts," *The Journal of Physical Chemistry*, vol. 90, no. 2, pp. 292–295, Jan. 1986. [Online]. Available: http://pubs.acs.org/doi/abs/10.1021/j100274a018

[9] X. Li, J. Yu, J. Low, Y. Fang, J. Xiao, and X. Chen, "Engineering heterogeneous semiconductors for solar water splitting," *Journal of Materials Chemistry A*, 11 2014. [Online]. Available: https://doi.org/10.1039/C4TA04461D

[10] Z. Chen, H. N. Dinh, and E. Miller, *Photoelectrochemical Water Splitting*, ser. SpringerBriefs in Energy. New York, NY: Springer New York, 2013. [Online]. Available: http://link.springer.com/10.1007/978-1-4614-8298-7

[11] C. Shakespeare, "Atomikerroskasvatetun titaanioksidiohutkalvon valokatalyyttisten ominaisuuksien parantaminen lämpökäsittelyllä," 5 2017.

[12] Q. Liu, D. Ding, C. Ning, and X. Wang, "Black Ni-doped TiO_2 photoanodes for high-efficiency photoelectrochemical water-splitting," *International Journal of Hydrogen Energy*, vol. 40, no. 5, pp. 2107–2114, Feb. 2015. [Online]. Available: https://linkinghub.elsevier.com/retrieve/pii/S0360319914034612

[13] X. Chen, L. Liu, P. Y. Yu, and S. S. Mao, "Increasing solar absorption for photocatalysis with black hydrogenated titanium dioxide nanocrystals," *Sciencexpress*, vol. 11, Jan. 2011.

[14] K. Kaur and C. V. Singh, "Amorphous TiO_2 as a photocatalyst for hydrogen production: a DFT study of structural and electronic properties," *Energy Procedia*, vol. 29, pp. 291–299, 2012.

[15] X. Zou and Y. Zhang, "Noble metal-free hydrogen evolution catalysts for water splitting," *Chemical Society Reviews*, 08 2015. [Online]. Available: https://doi.org/10.1039/c4cs00448e

[16] J. Ran, J. Zhang, J. Yu, M. Jaroniec, and S. Z. Qiao, "Earth-abundant cocatalysts for semiconductor-based photocatalytic water splitting," *Chem. Soc. Rev.*, vol. 43, no. 22, pp. 7787–7812, 2014. [Online]. Available: http://xlink.rsc.org/?DOI=C3CS60425J

[17] R. Liu, Z. Zheng, J. Spurgeon, and X. Yang, "Enhanced photoelectrochemical water-splitting performance of semiconductors by surface passivation layers," *Energy and Environmental Science*, 05 2014. [Online]. Available: https://doi.org/10.1039/c4ee00450g

[18] A. Kudo and Y. Miseki, "Heterogeneous photocatalyst materials for water splitting," *Chemical Society Reviews*, pp. 253–278, 11 2009.

[19] R. Fan, W. Dong, L. Fang, F. Zheng, and M. Shen, "More than 10% efficiency and one-week stability of Si photocathodes for water splitting by manipulating the loading of the Pt catalyst and TiO_2 protective layer," *Journal of Materials*

Chemistry A, vol. 5, no. 35, pp. 18 744–18 751, 2017. [Online]. Available: http://xlink.rsc.org/?DOI=C7TA04986B

[20] B. Streetman and S. Banerjee, *Solid State Electronic Devices*. Pearson, 2015.

[21] Y. W. Chen, J. D. Prange, S. Dühnen, Y. Park, M. Gunji, C. E. D. Chidsey, and P. C. McInture, "Atomic layer-deposited tunnel oxide stabilizes silicon photoanodes for water oxidation," *Nature Materials*, 06 2011. [Online]. Available: https://doi.org/10.1038/NMAT3047

[22] W. Wang, S. Liu, L. Nie, B. Cheng, and J. Yu, "Enhanced photocatalytic H_2 -production activity of TiO_2 using $Ni(NO_3)_2$ as an additive," *Phys. Chem. Chem. Phys.*, vol. 15, no. 29, pp. 12 033–12 039, 2013. [Online]. Available: http://xlink.rsc.org/?DOI=C2CP43628K

[23] P. D. Tran, L. Xi, S. K. Batabyal, L. H. Wong, J. Barber, and J. S. Chye Loo, "Enhancing the photocatalytic efficiency of TiO2 nanopowders for H2 production by using non-noble transition metal co-catalysts," *Physical Chemistry Chemical Physics*, vol. 14, no. 33, p. 11596, 2012. [Online]. Available: http://xlink.rsc.org/?DOI=c2cp41450c

[24] J. Zhao, T. M. Gill, and X. Zheng, "Enabling silicon photoanodes for efficient solar water splitting by electroless-deposited nickel," *Nano Research*, vol. 11, no. 6, pp. 3499–3508, Jun. 2018. [Online]. Available: http://link.springer.com/10.1007/s12274-018-2038-4

[25] J. R. McKone, E. L. Warren, M. J. Bierman, S. W. Boettcher, B. S. Brunschwig, N. S. Lewis, and H. B. Gray, "Evaluation of Pt, Ni, and Ni–Mo electrocatalysts for hydrogen evolution on crystalline Si electrodes," *Chemical Society Reviews*, no. 4, pp. 3573–3583, 08 2011.

[26] S. M. George, "Atomic Layer Deposition: An Overview," *Chemical Reviews*, vol. 110, no. 1, pp. 111–131, Jan. 2010. [Online]. Available: http://pubs.acs.org/doi/abs/10.1021/cr900056b

[27] A. R. Head, S. Chaudhary, G. Olivieri, F. Bournel, J. N. Andersen, F. Rochet, J.-J. Gallet, and J. Schnadt, "Near Ambient Pressure X-ray Photoelectron Spectroscopy Study of the Atomic Layer Deposition of TiO_2 on $RuO_2(110)$," *The Journal of Physical Chemistry C*, vol. 120, no. 1, pp. 243–251, Jan. 2016. [Online]. Available: http://dx.doi.org/10.1021/acs.jpcc.5b08699

[28] B. Abendroth, T. Moebus, S. Rentrop, R. Strohmeyer, M. Vinnichenko, T. Weling, H. Stöcker, and D. C. Meyer, "Atomic layer deposition

of TiO_2 from tetrakis(dimethylamino)titanium and H_2O," *Thin Solid Films*, vol. 545, pp. 176–182, Oct. 2013. [Online]. Available: https://linkinghub.elsevier.com/retrieve/pii/S0040609013012777

[29] Q. Xie, J. Musschoot, D. Deduytsche, R. L. Van Meirhaeghe, C. Detavernier, S. Van den Berghe, Y.-L. Jiang, G.-P. Ru, B.-Z. Li, and X.-P. Qu, "Growth Kinetics and Crystallization Behavior of TiO_2 Films Prepared by Plasma Enhanced Atomic Layer Deposition," *Journal of The Electrochemical Society*, vol. 155, no. 9, p. H688, 2008. [Online]. Available: http://jes.ecsdl.org/cgi/doi/10.1149/1.2955724

[30] T. Nam, J.-M. Kim, M.-K. Kim, H. Kim, and W.-H. Kim, "Low-temperature Atomic Layer Deposition of TiO_2, Al_2O_3, and ZnO Thin Films," *Journal of the Korean Physical Society*, 08 2011. [Online]. Available: https://doi.org/10.3938/jkps.59.452

[31] K. W. Kolasinski, *Surface Science: Foundations of Catalysis and Nanoscience*, 3rd ed. John Wiley & Sons, 2012.

[32] J. F. Moulder, W. F. Stickle, P. E. Sobol, and K. D. Bomben, *Handbook of X-ray Photoelectron Spectroscopy*. Perkin-Elmer Corporation, Physical Electronics Division, 1992.

[33] G. A. Somorjai and Y. Li, *Introduction to Surface Chemistry and Catalysis*, 2nd ed. John Wiley & Sons, 2010.

[34] M. C. Biesinger, B. P. Payne, A. P. Grosvenor, L. W. Lau, A. R. Gerson, and R. S. Smart, "Resolving surface chemical states in XPS analysis of first row transition metals, oxides and hydroxides: Cr, Mn, Fe, Co and Ni," *Applied Surface Science*, vol. 257, no. 7, pp. 2717–2730, Jan. 2011. [Online]. Available: http://linkinghub.elsevier.com/retrieve/pii/S0169433210014170

[35] M. C. Patt, *Bulk and surface sensitive energy-filtered photoemission microscopy using synchrotron radiation for the study of resistive switching memories*, ser. Schriften des Forschungszentrums Jülich Reihe Schlüsseltechnologien. Jülich: Forschungszentrum Jülich, 2016, no. Band 122.

[36] J. Walton and N. Fairley, *The Casa Cookbook Part 2: XPS Image Processing*. Acolyte Science, 2011.

[37] G. Margaritondo, "Photoelectron spectromicroscopy and spectronanoscopy at synchrotrons: Growing impact on life sciences and materials science," *Journal of Electron Spectroscopy and Related Phenomena*, vol. 178-179, pp. 273–291,

May 2010. [Online]. Available: http://linkinghub.elsevier.com/retrieve/pii/S0368204809001236

[38] C. D. Wagner, E. Davis, M. V. Zeller, J. A. Taylor, R. H. Raymond, and L. H. Gale, "Empirical Atomic Sensitivity Factors for Quantitative Analysis by Electron Spectroscopy for Chemical Analysis," *Surface and Interface Analysis*, 10 1981. [Online]. Available: https://doi.org/10.1002/sia.740030506

[39] E. Barsoukov and J. R. Macdonald, Eds., *Impedance Spectroscopy*. Hoboken, NJ, USA: John Wiley & Sons, Inc., Jan. 2005. [Online]. Available: http://doi.wiley.com/10.1002/0471716243

[40] M. Hannula, H. Ali-Löytty, K. Lahtonen, E. Sarlin, J. Saari, and M. Valden, "Improved Stability of Atomic Layer Deposited Amorphous TiO_2 Photoelectrode Coatings by Thermally Induced Oxygen Defects," *Chemistry of Materials*, vol. 30, no. 4, pp. 1199–1208, Feb. 2018. [Online]. Available: http://pubs.acs.org/doi/10.1021/acs.chemmater.7b02938

[41] A. Herrera-Gomez, D. Cabrera-German, M. Bravo-Sanchez, J.-A. Huerta-Ruelas, J.-H. Mata-Salazar, and G. Molar-Velazquez, "The satellites of the 2p core level of transition-metals," p. 13.

[42] H. B. Michaelson, "The work function of the elements and its periodicity," *Journal of Applied Physics*, vol. 48, no. 11, pp. 4729–4733, Nov. 1977. [Online]. Available: http://aip.scitation.org/doi/10.1063/1.323539

[43] M. Hannula, K. Lahtonen, H. Ali-Löytty, A. Zakharov, T. Isotalo, J. Saari, and M. Valden, "Fabrication of topographically microstructured titanium silicide interface for advanced photonic applications," *Scripta Materialia*, vol. 119, pp. 76–81, Jul. 2016. [Online]. Available: https://linkinghub.elsevier.com/retrieve/pii/S1359646216300902

[44] A. Zakharov, I. Batirev, and A. Narmonev, "X-ray photoelectron spectroscopy and calculation of the electronic structure in iron based alloys under phase transformation," *Solid State Communications*, vol. 46, pp. 739–742, 06 1983.

[45] Y. Cao, L. Nyborg, and U. Jelvestam, "XPS calibration study of thin-film nickel silicides," *Surface and Interface Analysis*, vol. 41, no. 6, pp. 471–483, Jun. 2009. [Online]. Available: http://doi.wiley.com/10.1002/sia.3050

[46] A. Novikov, "Experimental measurement of work function in doped silicon surfaces," *Solid-State Electronics*, vol. 54, no. 1, pp. 8–13, Jan. 2010. [Online]. Available: http://linkinghub.elsevier.com/retrieve/pii/S0038110109002494

[47] M. T. McDowell, M. F. Lichterman, A. I. Carim, R. Liu, S. Hu, B. S. Brunschwig, and N. S. Lewis, "The Influence of Structure and Processing on the Behavior of TiO_2 Protective Layers for Stabilization of n-Si/TiO_2/Ni Photoanodes for Water Oxidation," *ACS Applied Materials & Interfaces*, vol. 7, no. 28, pp. 15 189–15 199, Jul. 2015. [Online]. Available: http://pubs.acs.org/doi/10.1021/acsami.5b00379